AD-A146 343 HGCDTE SURFACE AND DEFECT STUDY PROGRAM(U) SANTA BARBARA RESEARCH CENTER GOLETA CALIF J A WILSON ET AL. JAN 84 SBRC-41514 MDA903-83-C-0108 1/2

UNCLASSIFIED F/G 20/12 NL

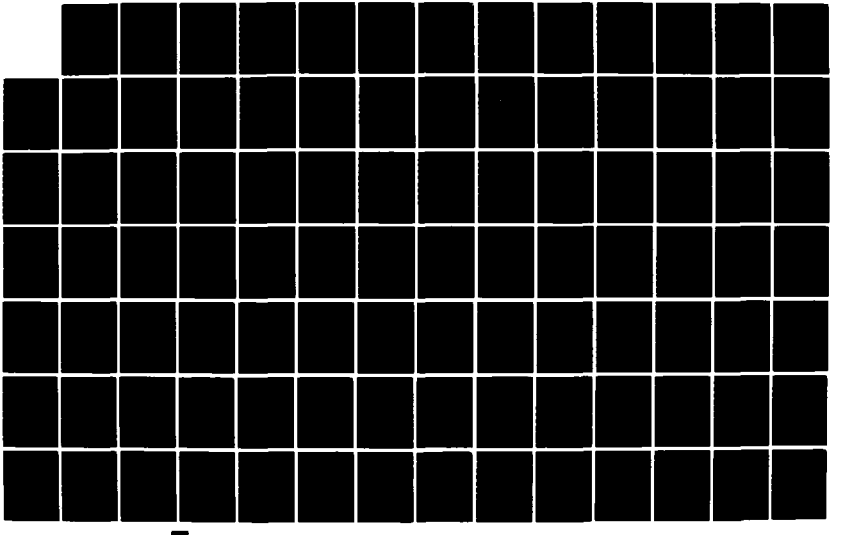

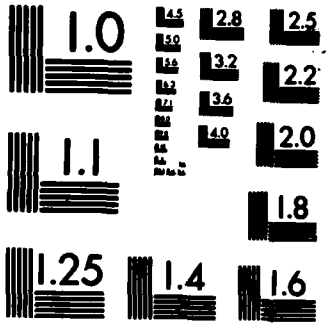

MICROCOPY RESOLUTION TEST CHART
NATIONAL BUREAU OF STANDARDS-1963-A

AD-A146 343

(12)

HgCdTe SURFACE AND DEFECT STUDY PROGRAM

J. A. Wilson and V. A. Cotton
Santa Barbara Research Center
Goleta, CA 93117

J. A. Silberman, G. Carey, D. Laser, S. Cole, C. Shih
D. J. Friedman, I. Lindau, and W. E. Spicer
Stanford Electronics Laboratories
Stanford, CA 94305

A. Sher
SRI International
Menlo Park, CA

R.G. Wilson
Hughes Research Laboratories
Malibu, CA

January 1984

SECOND INTERIM TECHNICAL REPORT

Contract No. MDA-903-83-C-0108

The views, opinions, and findings contained in this report are those of the authors and should not be construed as an official Department of Defense position, policy, or decision, unless so designated by other official documentation.

DTIC FILE COPY

Prepared for:
DARPA
1400 Wilson Blvd.
Arlington, Virginia 22209
Attention: Dr. Richard A. Reynolds
Material Science Division

DTIC
ELECTE
OCT 0 3 1984
S D
E

This document has been approved for public release and sale; its distribution is unlimited.

84 09 24 038

8a. NAME OF FUNDING/SPONSORING ORGANIZATION	8b. OFFICE SYMBOL (If applicable)	9. PROCUREMENT INSTRUMENT IDENTIFICATION NUMBER
DARPA		MDA-903-83-C-108

8c. ADDRESS (City, State and ZIP Code)	10. SOURCE OF FUNDING NOS.			
	PROGRAM ELEMENT NO.	PROJECT NO.	TASK NO.	WORK UNIT NO.
1400 Wilson Blvd. Arlington, CA 22209				
11. TITLE (Include Security Classification) HgCdTe Surface and Defect Study Program				

12. PERSONAL AUTHOR(S)
J.A. Wilson, V.A. Cotton, J.A. Silberman, G. Cary, D. Laser, S. Cole, (cont. on reverse)

13a. TYPE OF REPORT	13b. TIME COVERED	14. DATE OF REPORT (Yr., Mo., Day)	15. PAGE COUNT
Interim Technical	FROM 0783 TO 1283	840131	99

16. SUPPLEMENTARY NOTATION

17. COSATI CODES			18. SUBJECT TERMS (Continue on reverse if necessary and identify by block number)
FIELD	GROUP	SUB. GR.	HgCdTe, HgTe, CdTe, II-VI alloys, photoemission spectroscopy, surfaces, defects, electronic structure, interface

19. ABSTRACT (Continue on reverse if necessary and identify by block number)

This report presents program results, for the second six-month period ending December 31, 1983. The results presented include measurements of interface charge at the HgCdTe surface passivated with Photox™ SiO_2 as well as the surface work function; SIMS measurement of ^1H, ^2H and ^4He implanted into HgCdTe and CdTe, including third moment of the distribution; angle resolved photoemission studies of surface and bulk electronic structure; TEM examination of defects at the LPE HgCdTe/CdTe interface; measurement of surface oxidation and its effects on electronic structure; also presented are preliminary calculations of the binary bond lengths of various semiconductors including II-VI's and the effects of forming psuedo-binary alloys; vacancy formation energy and activation energy including effects of charge redistribution; and alloy hardness calculations.

(12) C.K. Shih, D.J. Friedman, I. Lindau, W.E. Spicer, A. Sher, R.G. Wilson

(18) states, DLTS, alloy bonding, alloy hardness, bond length, oxidation, capacitance, ion implantation, implant damage, channeled implant, TEM, passivation.

CONTENTS

Section		Page
	Summary	1
	Introduction	3
I	Interface Study	5
II	Channeled Implantation Study	21
III	Surface Study	35
IV	Alloy Bonding	73
	Acknowledgements	97

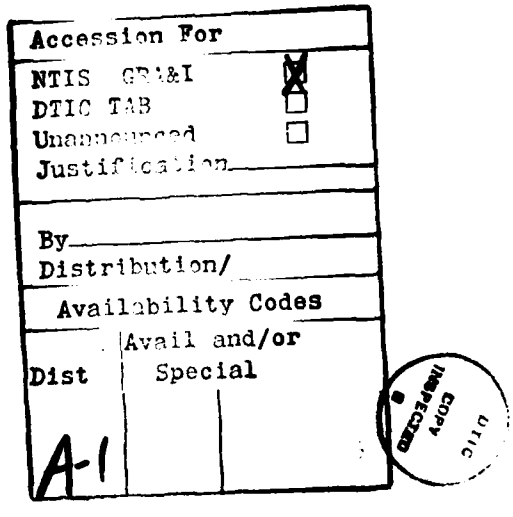

(This Page Intentionally Left Blank)

SUMMARY

Studies of the interface properties of MIS devices made with Photox™ SiO_2 on HgCdTe have shown that interface trap charge (Q_{it}) is an important contributor to net interface charge. In some cases it can dominate the fixed charge resident in the insulator. This indicates that the net interface charge which is the dominant surface effect on passivated detector properties, will be dependent on: pre-SiO_2 deposition surface treatments; water content; and surface fermi energy level ($E_{f,s}$) and therefore on doping density and temperature.

The implantation task has demonstrated an ability to detect atomic densities of ^1H, ^2H and ^4He in HgCdTe and CdTe above 10^{18} cm^{-3}. Cesium beam SIMS was used, and range parameters have been determined. This will be an important diagnostic tool for later examination of channeled He and H isotopes.

Angle resolved photoemission spectroscopy has been used to obtain a detailed description of the bulk HgCdTe electronic band structure. The electronic structure of the alloy at once accounts for the desired tunable bandgap of the materials as well as many materials problems in growth and preparation. These are necessary to explain the surface and interface properties affecting passivation as well as the LPE heterojunction interface. Results are also presented using TEM to examine this interface. Analysis of the imaged defects yields data on stacking fault energies and dislocation motion and annealing. Surface properties were probed directly in a comparative study of activated oxygen uptake on the clean (110) faces of CdTe, HgTe, and $Hg_{0.69}Cd_{0.31}Te$, and in a first attempt at learning more about the mechanism of surface type conversion observed upon cleavage by performing the cleaving at reduced temperature. Initial data regarding the kinetics of the oxidation process were obtained which augment information on the chemistry of the oxygen-HgCdTe interaction.

Bonding studies have concentrated on the calculation of important alloy properties. These include atomic term values, electron extraction energies, and many body excitation energies for all the group II, III, IV, V and VI elements which are important for tetrahedral semiconductors. Calculations are also in progress which will yield the bond energies and bond lengths of the "pure" semiconductor (binary) compounds and their modification in the pseudobinary alloy.

Harrison's theory of the shear coefficients has been extended to the calculation of dislocation energies in pure semiconductors and alloys, and a theory of alloy hardess based on detailed bonding is presented.

INTRODUCTION

This interim report presents results obtained in the second six-month period (ending December 31, 1983) of a three-year study of the interface region of HgCdTe. The effort is a collaboration of groups at Santa Barbara Research Center, Stanford University, SRI International, and Hughes Research Laboratories. The technical effort is divided into tasks to study: 1) interface properties which are important to device passivation; 2) surface effects and bulk defects due to ion implantation; 3) properties including defects of the free surface and defects of the alloy itself; and 4) theoretical analysis of bonding in random substitutional alloys as well as defect formation. Results of these tasks are presented in the following four sections of this report.

(This Page Intentionally Left Blank)

Section I
Interface Study

The purpose of the interface task is to determine the electronic characteristics of passivated interfaces concentrating on properties which have the greatest effect on device operation. We are concerned principally with operation of photovoltaic hetero- or homojunctions of the small size seen in large FPA applications. These are the applications where surfaces can have the dominant effect. As discussed in the previous interim report the principle impact on diode R_oA is due to interface charge which can produce a depletion layer at the HgCdTe surface. Interface charge is viewed as being due to a combination of fixed charge (in the dielectric), slow interface trap charge, and fast interface trap charge, depending on the response time of the particular states involved. These are indicated by a shift in flat band bias a voltage hysteresis (seen by comparing the voltage shift of the accumulation to inversion sweep with the return sweep), or a distortion of the slope of the high-frequency response through depletion.

The amounts of these types of charge vary strongly from device to device for what are nominally the same interface. For the case of Photox™ SiO_2 on HgCdTe, the SiO_2 is altered depending on (1) pressures and mixtures of the reactant gases, deposition rate, substrate temperatures; (2) the details of the surface preparation (i.e., whether a polish was used in conjunction with an etch or just an etch. This includes the nature and order in which chemicals were used; and (3) the amount and type of native oxide which is either formed or allowed to grow. All three of these have been shown to affect and alter interface charge so that in effect there is no generic SiO_2:HgCdTe interface. The properties of these interfaces are comparable one to another only when the surface preparation and manner of deposition of the SiO_2 is similar. For that reason and in order to form a meaningful data base we have adopted for this study a specific surface process and deposition procedure which is used for all our MIS devices.

The interface that results shows a very small voltage hysteresis compared to the other charge sources so that slow interface charge appears to be a second order effect. The interface trap contribution, as discussed in the appendix to this section, can be the dominant source of interface charge.

This has extremely important implications for the way in which SiO_2 behaves as a passivation in diode applications. Specifically, interface charge can be expected to be temperature and doping level dependent.

Interface trap distributions are believed to be due principally to scattering induced tailing of the conduction and valence bands into the gap at the surface. To first order then we can expect these to be essentially donor like (positively charged when unoccupied) and acceptor like (negatively charged when occupied). These trap densities are high at the band edges but decrease by several orders of magnitude by mid-gap so that the individual mid-gap contributions seem to give the values in the range of 10^{10} to 10^{12} cm^{-2} eV^{-1} that are measured. This is illustrated schematically in Figure 1. The most important aspect for determining the amount of charge under these conditions then is not so much the absolute value of D_{it} but its symmetry. A skewed distribution will mean that the higher values toward one band edge will not be as effective in cancelling the opposite charge of the other. Accurate calculation of this effect unfortunately depend on details of D_{it} in the region where it is least well characterized. However, meaningful estimates of the size of the effect can be made, as in the appendix, and do indicate the amount of Q_{it} is in the appropriate range to cause observed flat band shifts. For use as a passivation then on photovoltaic devices the net charge on the n and p side will be different. A process optimized for one side will not be necessarily be optimized for the other. The SiO_2 will act differently depending on the surface fermi energy. This is illustrated in Figure 1 where contributions to interfaces trap charge on n- and p-type surfaces are schematically represented. It becomes clear then that for effective passivation it is important to produce very low and very symmetrical distributions of interface traps. Symmetrical densities of less than 1×10^{10} $cm^{-1}ev^{-1}$ have been achieved on a handful of wafers so that it is not out of the question. Evidence also suggests this will greatly benefit 1/f noise levels as well as surface recombination velocity.

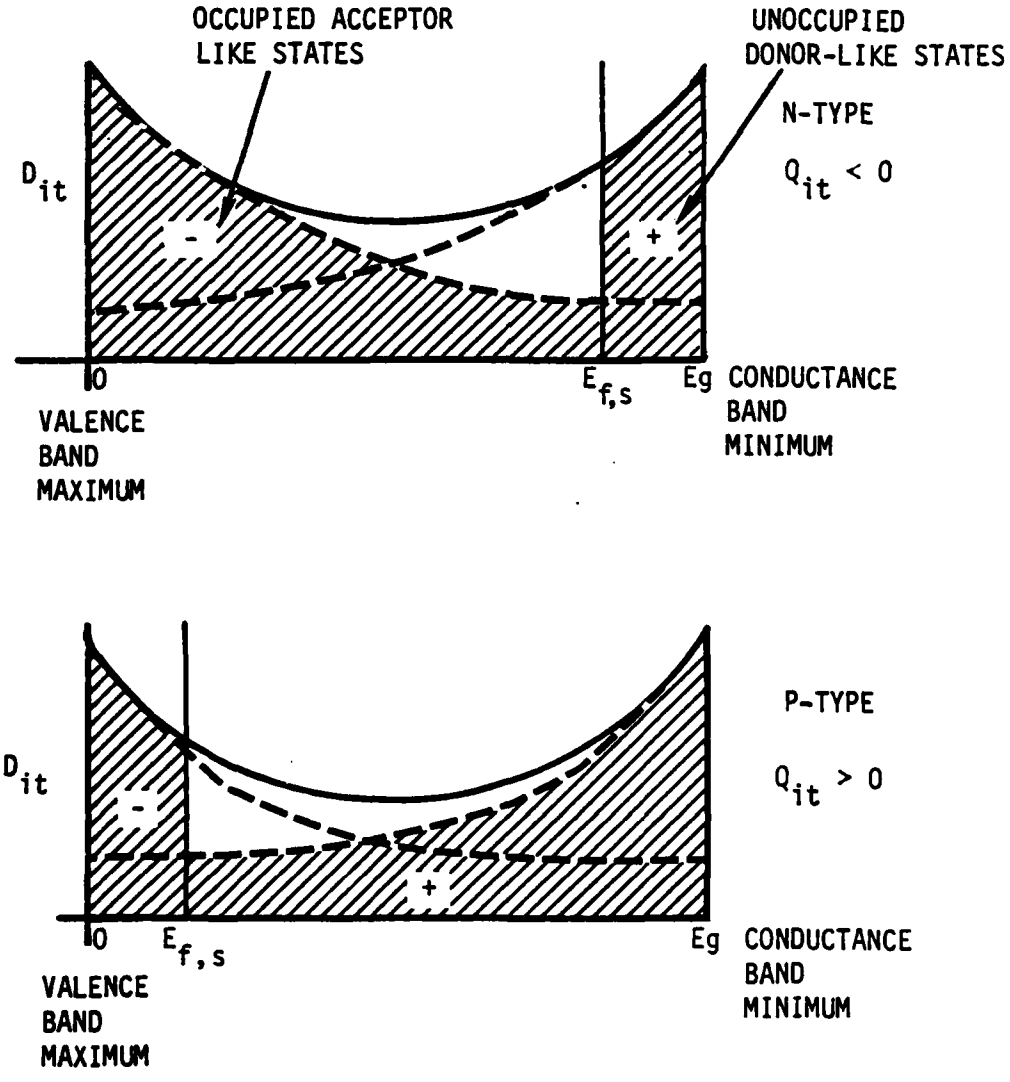

Figure 1. Schematic Representation of Contributions to Interface Trap Charge on n- and p-type Surfaces

ELECTRICAL PROPERTIES OF THE SiO_2:HgCdTe INTERFACE*

J.A. Wilson and V.A. Cotton

Santa Barbara Research Center, Goleta, CA 93117

By determining the dependence of flatband bias on insulator thicknesses in MIS devices made with PHOTOX™ SiO_2 on n-type $Hg_{0.7}Cd_{0.3}Te$ we have for the first time determined the amount of interface charge and the effective work function of the semiconductor surface. Flatband bias was determined from the surface potential as obtained by Berglund integration of quasi-static capacitance measurements at 77K. Insulator thickness was varied from 400 to 4000Å. The amount of fixed charge was seen to vary between -0.3×10^9 cm^{-2} and $+8 \times 10^{10}$ cm^{-2} depending on the type of deposition sequence used. It was also seen that H_2O could be absorbed into the layer and removed by vacuum baking at temperatures of 60 to 100°C and resulted in a change of interface fixed charge of up to 8×10^{10} cm^{-2}. This is in agreement with the range of charge variation seen above. The presence of large amounts of H_2O also was seen to introduce surface states at 0.06 and 0.14 eV above the valence band edge. (E_g = 0.26 eV at 77K). The effective work function difference between the Ti, Au bilayer gate and the HgCdTe surface was determined to be +0.03V ±0.05V.

INTRODUCTION

PHOTOX™ SiO_2 has become an important material for use in passivating HgCdTe photovoltaic devices in recent years. The net charge associated with these types of interfaces is the dominant parameter determining its effectiveness. PHOTOX™ is a form of low-temperature chemical vapor deposited (LTCVD) SiO_2. These types of SiO_2 are achieved by reacting silane (SiH_4) with oxygen

*Supported by DARPA Contract MDA-903-83-C-0108.

where different processes use different techniques for obtaining the oxygen. The PHOTOX™ process uses Hg vapor excited by exposure to UV (2547Å) radiation which catalyzes the decomposition of nitrous oxide (N_2O) to produce oxygen with H_2O as one of the by-products.[1] The emphasis in exploring these processes is that the HgCdTe alloy is intolerant of temperatures in excess of 100°C. Due also principally to their low deposition temperatures, the SiO_2 which results can be very different from the SiO_2 grown on Si by a higher temperature process.

EXPERIMENT

The interface with $Hg_{0.7}Cd_{0.3}Te$ has been characterized using MIS capacitors made on wafers cut from ingots grown by the horizontal zone melt technique. These wafers were cut parallel to the long axis of the ingot without regard to crystal orientation. They were then isothermally annealed in Hg vapor to lower the cation vacancies to less than 5×10^{13} cm^{-3} so that the final electrical activity is determined by residual impurities. This is usually n-type in the range of 1×10^{14} to 1×10^{15} cm^{-3}. Since only the outer 4-5 mils are affected many commonly present acceptors which are also fast diffuses in HgCdTe are gettered to the unannealed wafer core[2] and do not contribute to the surface region electrical properties.

Capacitors are then made by depositing PHOTOX™ SiO_2 followed by a gate metal. The gate is done by thermal evaporation through a shadow mask and consists of a thin Ti layer (400Å) followed by 5000Å of Au. Ground contact to the n-type HgCdTe is made with In solder.The insulator thickness was varied from 500Å to 4000Å in four steps. These sets of devices were then characterized by high (1M Hz) and low frequency (10^{-2} Hz) capacitance measurements. The data was reduced to give flat band bias and interface trap density. The

flatband bias is expected to vary in a characteristic manner with insulator thickness depending on the distribution of net interface charge. For the case of charge residing in a sheet near the interface the dependence is

$$V_{fb} = - \frac{Q_{fix} + Q_{it}}{C_{ins}} + W_{ms}$$

where the insulator capacitance is given by

$$C_{ins} = \frac{\varepsilon A}{d}$$

ε is the dielectric constant of the insulator $\left(5 \times 10^{-13} \frac{Fd}{cm}\right)$, A is the area ($2.04 \times 10^{-3}$ cm^2) and d is the thickness. Q_{fix} and Q_{it} are the fixed charge and interface trap charge. Taken together these are the net interface charge. W_{ms} is the effective work function difference between the metal gate and the semiconductor. We see that for this case we have a linear dependence of V_{fb} on net charge. By measuring V_{fb} at different thicknesses the net charge can be measured from the slope and the effective work function difference from the zero thickness intercept. Distributions of charge other than a sheet at the interface will of course show nonlinear dependence.[3]

The flatband bias is determined from plots of surface potential (Ψ_s) versus applied bias obtained by Berglund integration of quasi-static C-V curves[4]. These are compared to measurements of the shift of high frequency curves from ideal where no distortion of the high frequency curve in depletion occurs.

The insulator was deposited by two significantly different procedures. In one case a single wafer was coated with successive thin (500Å) depositions of SiO_2 on successively smaller areas of the wafer. The first deposition

covered the entire wafer and defined the interface region for all different thickness devices. Thicker devices then built up with up to four SiO_2 layers each separately deposited. The other procedure used separate smaller wafers cut from a larger single wafer, each separately coated with a single layer of appropriate thickness. The devices produced in this way are different in that the first layer and the interface have seen process steps and conditions which the single layer devices have not. Specifically they were exposed to the high temperatures (100°C) and vacuum (1×10^{-3} torr) of the predeposition PHOTOX™ chamber.

RESULTS

The results for these two types of layers show interesting differences. As shown in Figure 1, the data falls into two groups, both of which are reasonable fits to linear thickness dependence. The multilayer set of samples shows a small positive slope indicating a net charge of -3×10^{9} cm^{-2}. The single layer samples show a larger positive charge of $+8 \times 10^{10}$ cm^{-2}. The zero thickness intercepts for both sets of data, are essentially equivalent considering the scatter in the data for the assumption of linear thickness dependence. Thus it is clear that the charge at these interfaces is well characterized by a sheet very near the actual interface.

The amount of interface trap charge contributing to the net charge can be estimated from the apparent interface trap density (D_{it}) derived by taking either the difference between high and low frequency C-V curves[5] or the difference between experimental and ideal curves[3]. Results are shown in Figure 2. Also shown are estimated contributions from scattering induced tailing of the conduction and valence bands into the surface energy gap. States in the upper half of the gap are taken as donorlike (positively charged when unoccu-

pied) while those in the lower half as acceptorlike (negatively charged when occupied). An upper limit to the net interface trap charge at flatband is thus seen to be on the order of -1×10^{10} cm^{-2}. This is a small negative charge on the order of that seen in the multilayer sample and thus can be a significant contribution to layers low in absorbed water. This method of estimating interface trap charge is intended only to indicate an order of magnitude. Further, this value should be taken only as an upper limit, since the existence of any nonuniformities in either Q_{fix} or Q_{it} will make the apparent interface trap density appear artificially high. These nonuniformities also produce structure in D_{it}, especially in the region of $E_{f,s}$. This is the source of the drop off in D_{it} seen near the band edges in Figure 2.[6]

The difference in deposition sequence between the two types of devices is significant in a way which can account for the difference in net fixed charge. For the multilayer samples the chamber was opened to move the shutter then reevacuated ($\sim 1 \times 10^{-3}$ torr) for the next run. This gives each layer a 15 minute vacuum bake at 100°C. The single layer samples do not see this step.We have found that exposing single layer (1500Å thick) MIS devices to H_2O vapor (90% humidity, 24 hours at 32°C) and then vacuum bakes (on the order of 60°C for 12 hours) can shift the capacitance voltage curves by about -0.8V, corresponding to a change in net charge of $+8 \times 10^{10}$ cm^{-2}, equivalent to the difference in the two slopes in Figure 1. This is illustrated in Figure 3. These vacuum bakes are much longer than those associated with predeposition system purging but they are also at a significantly lower temperature and done on much thicker layers (1500Å compared to 500Å). The baked devices were also completed, with metal gates deposited on the SiO_2. While the first layer of the multilayer samples have, at this stage, an uncoated surface. This suggests that water does play a major role in the net charge seen in PHOTOX™

SiO_2. Although the exact mechanism is to be determined, water has been seen to play a number of important roles in PHOTOX™ in addition to the effects on net charge.[7]

Specifically the presence of H_2O due to high humidity exposure reversibly alters the interface trap distribution (D_{it}) as illustrated in Figure 4. This change in D_{it} is always associated, in these samples, with the above mentioned shift in V_{fb} by about one volt toward the negative corresponding to the positive change in net charge. Assigning this change as due to a change in Q_{it} requires the nature of D_{it} in the region of the peaks at 0.06 and 0.12 eV to change from acceptor to donor like. These are of course filled and therefore neutral. However there are then less filled acceptor like states (negative charge) to compensate the unfilled donor like states (positive charge) above E_{fs} resulting in the increase in positive contributions to Q_{it}.

The intercept with the vertical axis in Figure 1 is a measure of the effective work function difference between the $Hg_{0.7}Cd_{0.3}Te$ surface and the Ti/Au gate we see that W_{ms} = +0.03V ± 0.05V. The surface thus has very nearly the same work function as Ti (4.4 eV)[8] and is consistent with a previous measurement made at the anodic oxide interface by Nemirosky.[9] These wafers are n type at 1×10^{14} cm^{-3}, the bulk fermi energy is 0.213 eV and the energy gap at 77K is 0.243 eV. So that within our experimental tolerances the electron affinity for this surface is essentially 4.4 eV.

CONCLUSIONS

It is clear that at the PHOTOX™ SiO_2 HgCdTe interface the net interface charge (interface trap charge plus fixed charge) residues in a sheet very near the interface. The amount of net charge can vary through changes in the nature of charged interface traps. The actual fixed charge component appears

to be a very small amount of negative charge on the order of -1×10^{10} CM^{-2}. Finally the $Hg_{0.7}Cd_{0.3}Te$ electron affinity is estimated at 4.4 eV.

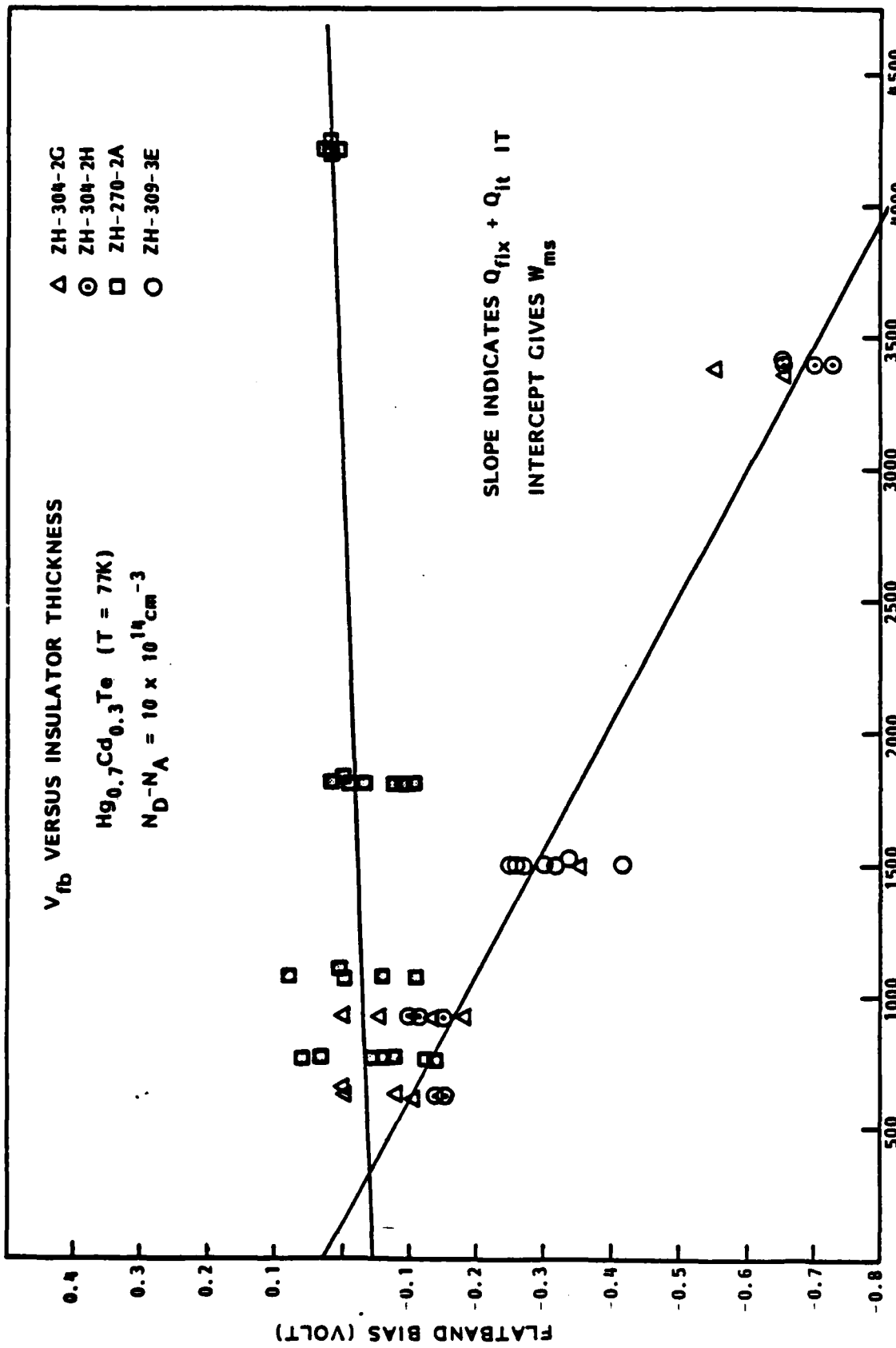

Figure 1. Flatband bias dependence on insulator thickness for both single and multilayer devices.

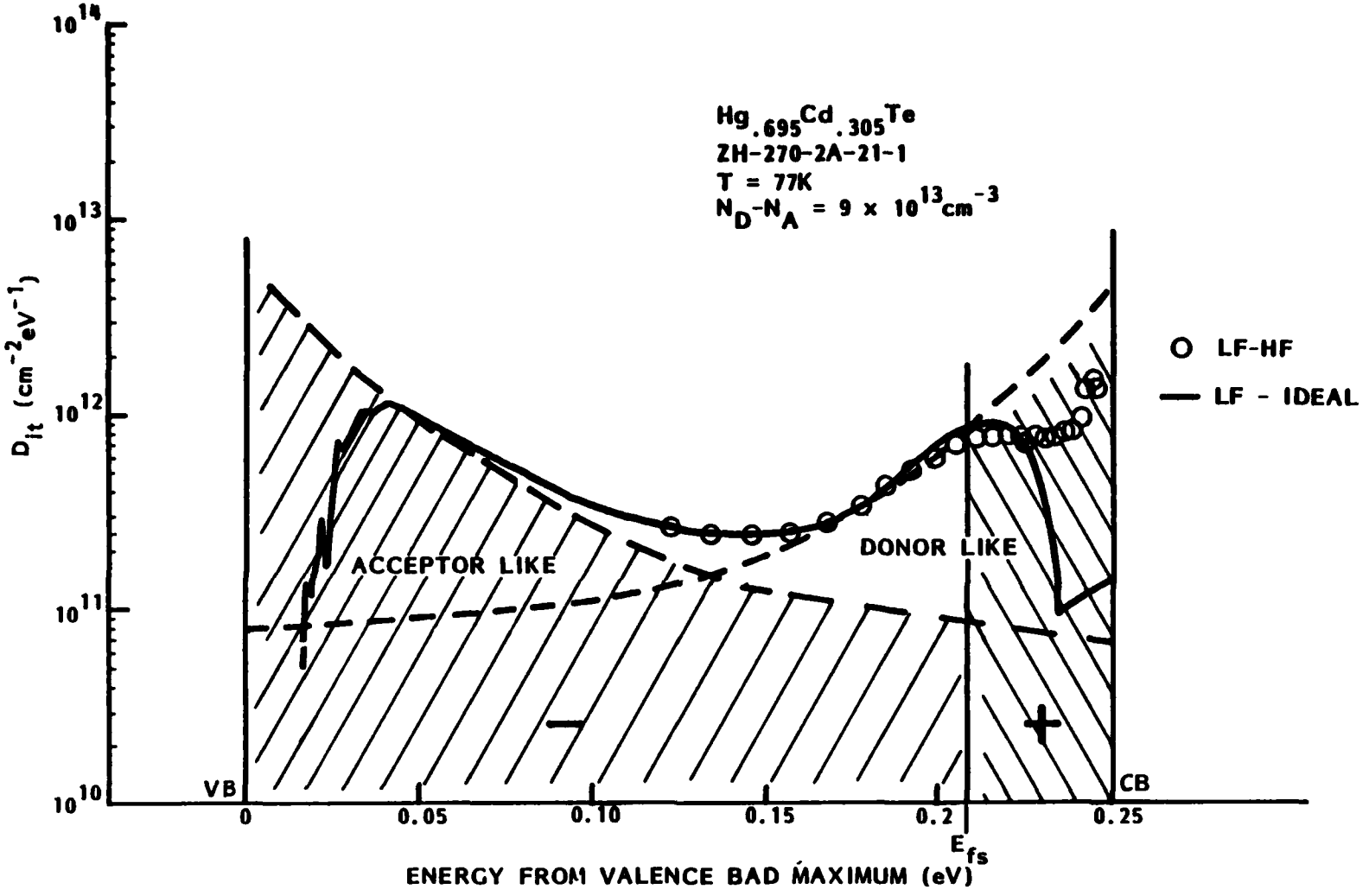

Figure 2. Density of interface traps (D_{it}) derived from low frequency measurements and calculated response (Ideal) and low frequency and high frequency measurements. Superimposed are estimated components due to valence and conduction band tailing. Shaded areas show charged contributions.

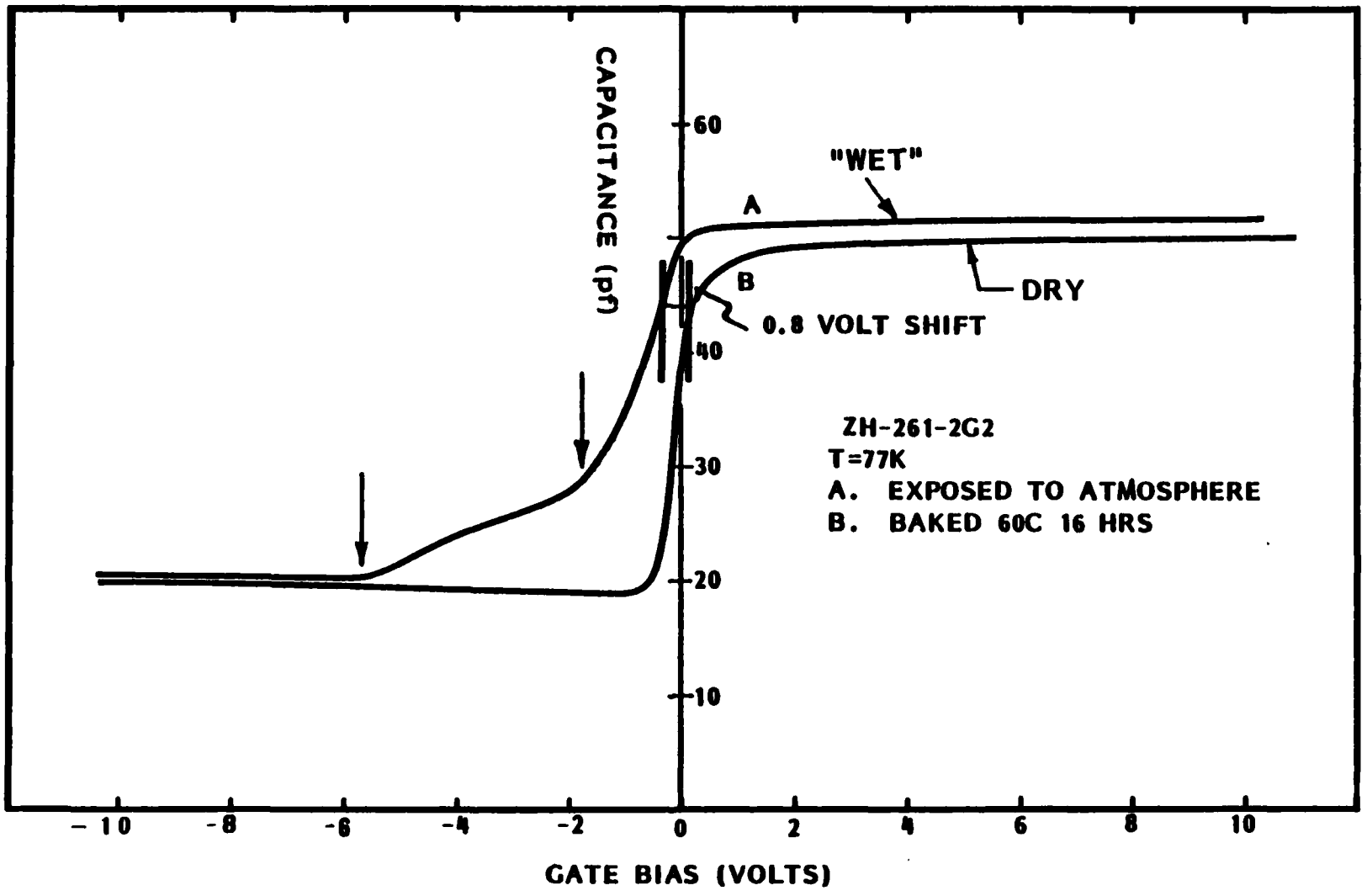

Figure 3. Effect of H_2O on high frequency capacitance measurement. Shows "water knee" (arrows) and resulting flatband bias shift.

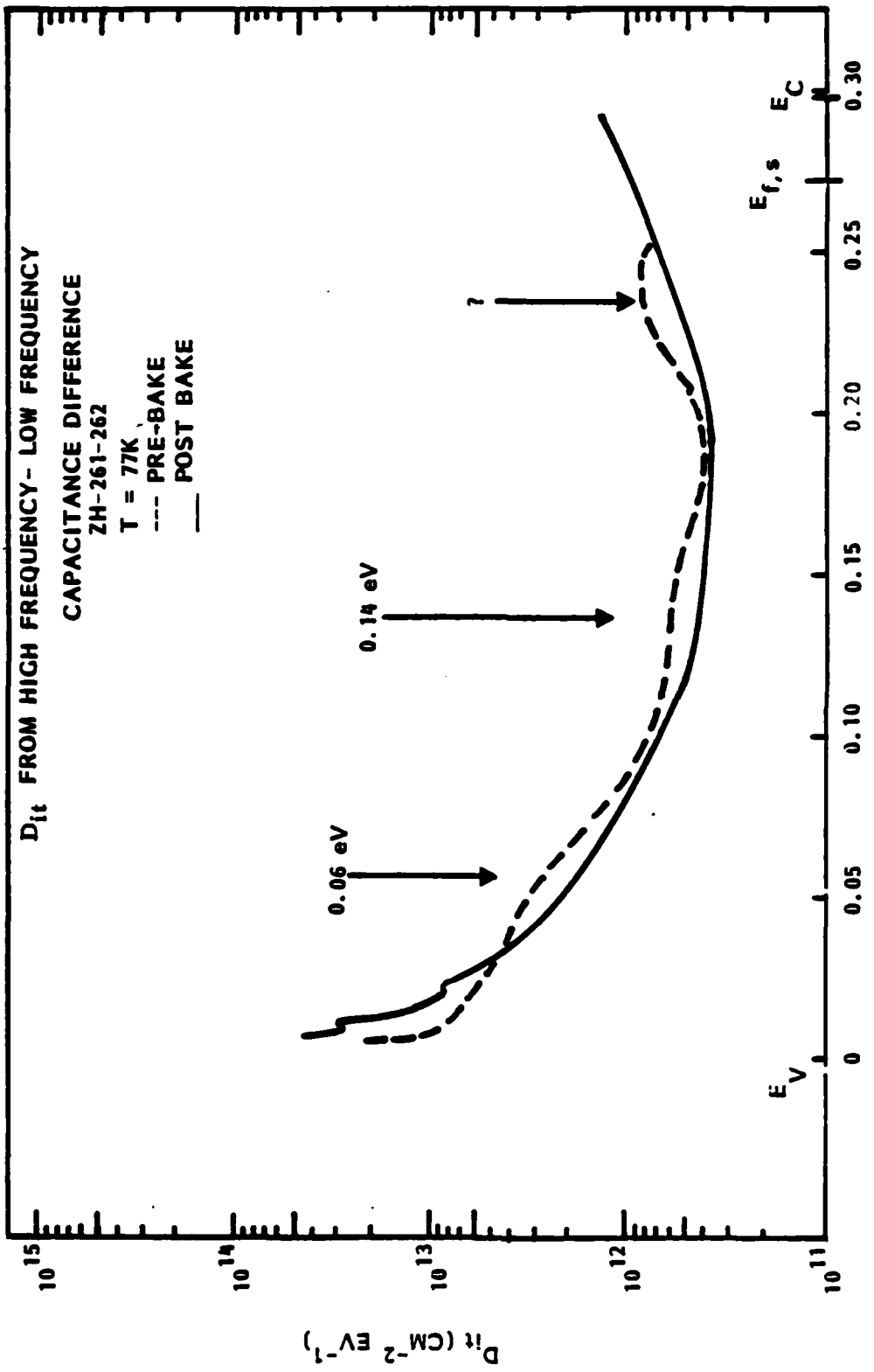

Figure 4. Alteration of fast interface trap distribution (D_{it}) due to presence of H_2O.

REFERENCES:

1. J.W. Peters, N.H. Rogers, J.T. Hall, E.M. Yee and D.R. Rhiger. Paper No. 202 Electro-chemical Society Meeting, 9-14 May 1982, Montreal, Canada.

2. J. Tregilgas, J. Beck and B. Gnade "Type-conversion of (HgCd)Te Induced by the Redistribution of Residual Acceptor Impurities". Paper delivered at the 1984 U.S. Workshop on the Physics and Chemistry of HgCdTe, May 15-17, 1984, San Diego, CA.

3. A.S. Grove. Physics and Technology of Semiconductor Devices, J. Wiley & Sons, New York (1967) p. 281.

4. C.N. Berglund, IEEE Trans. Electron Devices, ED-13, 701 (1966).

5. R. Cartagne and A. Vapaille, Surface Science 28, 557 (1971).

6. R. Cartagne and A. Vapaille, Surface Science 21, (197) 157-193.

7. J.A. Wilson and V.A. Cotton "Effects of H_2O on the SiO_2/HgCdTe interface". Submitted to J. Appl. Phys.

8. H.B. Michaelson, IBM J. Res. Dev., 22, 72 (1978).

9. Y. Nemirovsky and I. Ki-dron Solid State Elect., 22, 831 (1979).

(This Page Intentionally Left Blank)

Section II
Channeled Implantation

Section II-1

As discussed in the introduction to the first interim report, there is a distinct difference in the effects on device performance of interface charge depending on whether the device involves ion implantation or not. These data taken on the effects of gate bias on the junction region of LPE-grown double layers were compared to ion implanted devices. For nominally similar devices the R_oA of implanted junctions is lower than double-layer junctions. MIS devices on B+ implanted surfaces have been seen to exhibit higher thermal generation rates than unimplanted but similarly doped material. It appears a deep state is introduced by ion implantation which adversely affects the surface region and therefore device performance. It is well documented that the resultant n-type doping resulting from ion implantation into HgCdTe is a result of electrically active damage sites so that the nature of the specific ion is largely irrelevant. These effects occur for random implants where each ion-lattice collision can transfer a large portion of the ion kinetic energy. It is possible to implant into the (110) face where the zinc blend structure presents open channels. In this case the probability of direct collision with a lattice site except at the crystal surface is low. Ions channeled in this way will lose energy to the lattice by interaction of their electron clouds. The "nuclear" component of energy loss, believed responsible for the lattice damage, will only be probable very near the end of the ion range where the ion kinetic energy is low and less likely to cause damage. This technique is being pursued as a means to produce electrically active regions without the usual n-type damage. Of particular interest are ions of isotopes of H and He. These have proven, however, very difficult to detect once implanted. In this section we report a demonstration of a technique used to detect these ions in HgCdTe and CdTe.

Section II-2

Depth distributions of ^{1}H, ^{2}H, and ^{4}He implanted into HgCdTe and CdTe measured by secondary ion mass spectrometry

R. G. Wilson, Hughes Research Laboratories, Malibu, CA 90265

Abstract

The capability to measure atom densities of ^{1}H, ^{2}H, and ^{4}He in HgCdTe and CdTe above about 10^{18} cm^{-3} in background-subtracted cesium beam secondary ion mass spectrometry profiles has been demonstrated using ion implantation and implanted fluences. Range parameters are determined for ion energies between 150 and 300 keV. Projected ranges for ^{1}H are slightly greater than those for ^{2}H in both HgCdTe and CdTe. Hydrogen ion ranges are about 0.75 μm/100 keV of energy in both materials, and the third moment of the depth distributions is about -2.1.

In 1971, Foyt, Harman, and Donnelly[1] reported the fabrication of n-p junction photodiodes in $Hg_{1-x}Cd_xTe$ (x = 0.2 - 0.5) by the implantation of protons of 100 keV energy and 1 to 5 x 10^{14} cm^{-2} fluences. Electrical performance parameters were reported, which included the observation that the n layer created by the proton bombardment was about 1 μm thick, but no information about the depth of penetration of the 100-keV protons or the depth profile or density of the implanted hydrogen atoms was given. No work has been subsequently reported about the implantation of hydrogen or helium ions in HgCdTe although considerable work has been reported[2-14] using heavier ions, especially boron.[2-11] Of the 10 papers that used B implantation, four measured the B depth distribution by using secondary ion mass spectrometry (SIMS) profiling.[2-5] N-type regions are frequently reported to be produced by implantation (damage) irrespective of which ion is implanted, and the n regions are deeper than the implanted ion ranges.

In 1967, Smirnov and Kachurin et al.[15,16] reported electrical effects of implanting Cd and In into CdTe. Donnelly et al.[17] reported type conversion and the formation of p-n junctions by the implantation of 400-keV As into n-CdTe. Subsequently, others reported[18-20] the results of implanting heavy ions into CdTe. No work has been reported in which the light ions H or He have been implanted into CdTe.

Implantation ranges are shallow for heavy ions in the high atomic number substrates HgCdTe and CdTe. The surfaces of these materials, especially HgCdTe, are subject to effects caused by

defects and vacancies. Light ions (e.g., H and He) cause fewer defects and penetrate more deeply than heavy ions. Light ions therefore may be useful for creating deeper n-p junctions in either HgCdTe or CdTe, as Foyt et al. reported for 100 keV protons. We have implanted the light ions ^{1}H, ^{2}H, and ^{4}He into HgCdTe and CdTe at energies from 150 to 300 keV and profiled their depth distributions using SIMS. We have performed Pearson IV fits on these depth distributions and report the peak ranges R_m, the projected ranges R_p (μ), the range straggles ΔR_p (σ), the skewness or third moment, and the kurtosis or fourth moment, that is, the four moments of the depth distributions, and the doping densities achieved. This is the first time that profiles for H or He impurities in HgCdTe or CdTe have been reported. These results also indicate that hydrogen (as ^{1}H or ^{2}H) can be profiled as an impurity in HgCdTe or CdTe by secondary ion mass spectrometry, if the H atom density is greater than about 5×10^{18} cm^{-3}.

Implantation into HgCdTe and CdTe was performed as it is for Si, GaAs, and other semiconductors. Samples of (111) horizontal zone refined and (111) LPE HgCdTe on CdTe substrates and of the semi-insulating CdTe substrates themselves were implanted with ^{1}H, ^{2}H, and ^{4}He ions at energies between 150 and 300 keV, fluences of 10^{14}, 10^{15}, and 10^{16} cm^{-2}, and at current densities of $\sim 10^{-7}$ A cm^{-2} at room temperature. The samples were tilted 7^{o} from the surface normal to minimize channeling. Implantation energies are accurate to within about 2% and fluences, to within about 10%.

Establishing a SIMS technology for profiling hydrogen and helium in HgCdTe and CdTe required special effort because their ionization potentials are high, their electron affinities are low, and H is present in the vacuum ambient. Profiles could not be obtained for the 10^{14} cm^{-2} implant fluences in either material, and only for the 10^{16} cm^{-2} He fluence in HgCdTe. We were not successful with He in CdTe even for the 10^{16} cm^{-2} fluence, probably because of the semi-insulating nature of the CdTe and the associated slight charging difficulties. The semi-insulating CdTe samples were coated with about 40 nm of Au to minimize charging during SIMS profiling. ^{1}H and ^{2}H were profiled using Cs ion bombardment and negative ion spectrometry. Helium was profiled using oxygen ion bombardment and positive ion spectrometry. Sputtering rates of about 10 nm/s were used. Background-subtracted detection limits (atom densities) of $\sim 10^{18}$ cm^{-3} were achieved for ^{1}H and ^{4}He, and $\sim 10^{17}$ cm^{-3} for ^{2}H. The SIMS measurements were carried out using a CAMECA IMS 3f instrument at Charles Evans and Associates. The atom densities were determined by equating the integral of the profile to the implanted fluence. The depth scales were obtained by measuring the SIMS crater depths using a surface profilometer (Dektak) and the crater depths are accurate to about $\pm$ 7%.

The depth distributions of ^{1}H and ^{2}H in HgCdTe are shown in Figure 1 and in CdTe, in Figure 2. The profile for He in HgCdTe is shown in Figure 3. Pearson IV fitting was performed on all profiles. The values of the maximum atom density N_{max}, depth at the maximum R_m, the projected range R_p (or μ), the range straggle

ΔR_p (or σ), the skewness γ_1, the kurtosis, β_2, and the relative kurtosis β_2' are given in Table I. The profiles for ^1H and ^2H were measured in the same SIMS profile, so their relative depths are subject to the 2% energy inaccuracy, not the $\pm$ 7% crater depth inaccuracy. The range of ^1H or ^2H in either material is approximately 0.75 μm per 100 keV of H ion energy. The third moments for H in both materials are moderately negative (~ -2), consistent with theory for light ions in high atomic number substrates. The statistics were poorer in the data for H in CdTe, so we show the actual data points and how we chose to draw the depth distribution curve through them in Figure 3. The statistics for H in HgCdTe were good enough to clearly define the curves shown in Figure 1.

Calculations of projected range R_p have been made for H in CdTe by Gibbons et al.[21] using the Lindhard, Scharff, and Schiøtt formalism. Their calculated values of R_p and ΔR_p for 150 keV H in CdTe are 1.40 and 0.30 μm, respectively; our experimental values for HgCdTe are 1.11 and 0.31 μm, respectively. Their values for 300 keV H in CdTe are 2.78 and 0.40 μm, respectively; our experimental values for CdTe are 2.15 and 0.33 μm for ^1H and 1.96 and 0.44 μm for ^2H, and for HgCdTe, our experimental values are 2.35 and 0.64 μm for ^1H. The differences between calculated and experimental values is within 20 or 30%. This is very good agreement for the large difference in atomic number between ion (1) and substrate ($\sim$ 50).

Foyt et al.[1] reported an n region created in HgCdTe by 100 keV proton implantation that was about 1 μm deep. We have shown

here that for 100 keV protons the R_p of the distribution should be about 0.75 μm and that the depth distribution would be about 1 m deep about one decade below the peak of the depth distribution on the deep side of the distribution, in good agreement with the n region reported by Foyt et al., assuming that carrier removal and/or doping effects of defects/damage are caused by implanted protons at densities down about one decade from the value of the peak of the implanted proton depth distribution, which should be between 2×10^{18} and 1×10^{19} cm^{-3} based on their fluence of 1 to 5×10^{14} cm^{-2} and our experimental profiles.

The work was supported by the Materials Sciences Office of DARPA under contract number MDA-903-83-C-0108. We are grateful to R. A. Reynolds for encouragement and support. J. A. Wilson of Santa Barbara Research Center supplied much of the material used and we are grateful for his encouragement also.

References

1. A. G. Foyt, T. C. Harman, and J. P. Donnelly, Appl. Phys. Lett. 18, 321 (1971).
2. L. O. Bubulac, W. E. Tennant, S. H. Shin, C. C. Wang, M. Lanir, E. R. Gertner, and E. O. Marshall, Japn. J. Appl. Phys. 19, Suppl. 19-1, 495 (1980).
3. J. Baars, A. Hurrle, W. Rothemund, C. R. Fritzsche, and T. Jacobus, J. Appl. Phys. 53, 1461 (1982).
4. S. Y. Wu, W. J. Choyke, W. J. Takei, A. J. Noreika, and M. H. Francombe, J. Vac. Sci. Technol. 21, 255 (1982).
5. K. L. Conway, W. G. Opyd, M. E. Greiner, J. F. Gibbons, T. W. Sigmon, and L. O. Bubulac, Appl. Phys. Lett. 41, 750 (1982).
6. S. Margalit, Y. Nemirorsky, and I. Rotstein, J. Appl. Phys. 50, 6386 (1979).
7. G. Bahir and R. Kalish, Appl. Phys. Lett. 39, 730 (1981).
8. G. Bahir and R. Kalish, and Y. Nemirovsky, Appl. Phys. Lett. 41, 1057 (1982).
9. L. O. Bubulac, W. E. Tennant, R. A. Riedel, and T. J. Magee, J. Vac. Sci. Technol. 21, 251 (1982).
10. L. K. Vodopaynov and S. P. Kozyrev, Phys. Stat. Sol. (a) 72, K133 (1982).
11. P. G. Pitcher, P. L. F. Hemment, and Q. V. Davis, Electron. Lett. 18, 1090 (1982).
12. L. K. Vodopyanov and S. P. Kozyrev, Phys. Stat. Sol. (a) 72, 737 (1982).
13. L. K. Vodopyanov, S. P. Kozyrev, and A. V. Spitsyn, Sov. Phys.-Semicond. 18, 626 (1982).

14. G. Bahir and R. Kalish, J. Appl. Phys. 54, 3129 (1983).

15. L. S. Smirnov, G. A. Kachurin, A. E. Gorodetskii, Sov. Phys. - Solid State 9, 564 (1967).

16. G. A. Kachurin, A. E. Gorodetskii, Yu. Loburets, and L. S. Smirnov, Sov. Phys. - Solid State 9, 375 (1967).

17. J. P. Donnelly, A. G. Foyt, E. D. Hinkley, W. T. Lindley, and J. O. Dimmock, Appl. Phys. Lett. 12, 303 (1968).

18. M. Gettings and K. G. Stephens, Radiat. Effects 18, 275 (1973).

19. J. C. Bean, Stanford Univ. Report SU-SSEL-76-002 (Thesis), 1976.

20. C. B. Norris, C. E. Barnes, and K. R. Zanio, J. Appl. Phys. 48, 1659 (1977).

21. J. F. Gibbons, W. S. Johnson, and S. W. Mylroie, Projected Range Statistics Semiconductors and Related Materials (Halstead, Wiley, New York, 1975).

Table I. Experimental range parameters for ^{1}H, ^{2}H, and ^{4}He in HgCdTe and CdTe

Ion	Ion energy keV	Ion fluence 10^{16} cm^{-2}	N_{max} 10^{20} cm^{-3}	R_m μm	R_p, μ μm	ΔR_p, σ μm	γ_1 Skewness	β_2 kurtosis	β_2' relative kurtosis
HgCdTe									
^{1}H	150	5.0	9.5	1.26	1.11	0.31	-2.2	17.8	7.1
^{2}H	150	5.0	9.0	1.33	1.18	0.30	-2.1	16.5	6.2
^{1}H	300	1.0	0.9	2.63	2.35	0.64	-2.3	15.6	4.5
^{2}H	300	1.0	0.9	2.71	2.23	0.65	-2.1	12.7	2.4
^{4}He	250	1.0	0.9	2.20	2.10	0.45	-0.36	3.6	0.3
CdTe									
^{1}H	300	1.0	1.3	2.33	2.15	0.33	-2.0	14	4
^{2}H	300	1.0	1.1	2.20	1.96	0.44	-1.8	9.8	1.1

Figure Captions

Figure 1. Depth distributions (measured using SIMS) of hydrogen implanted into HgCdTe.

Figure 2. Depth distribution (measured using SIMS) of helium implanted into HgCdTe.

Figure 3. Depth distributions (measured using SIMS) of hydrogen implanted into CdTe.

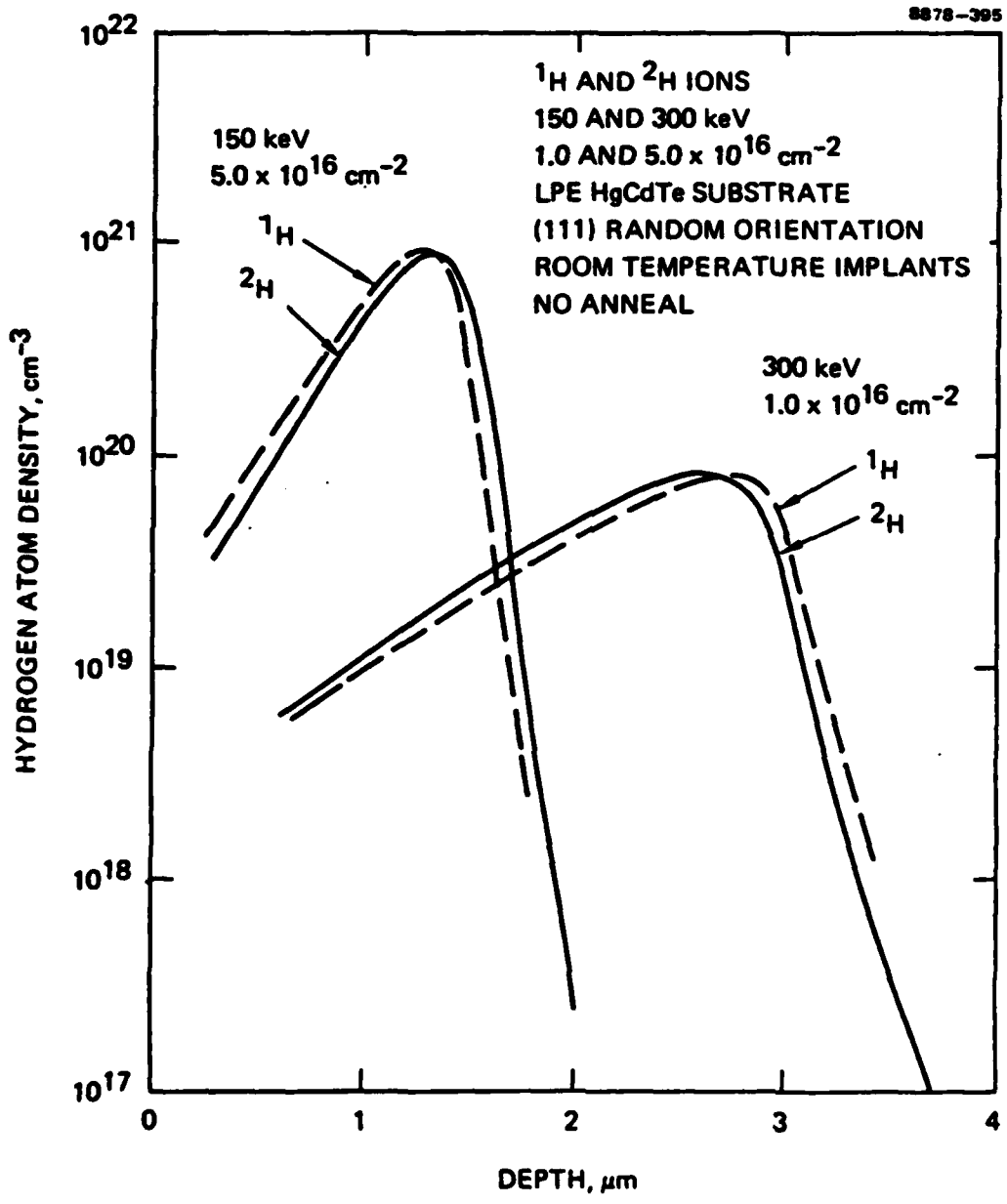
8878-395
^{1}H AND ^{2}H IONS
150 AND 300 keV
1.0 AND 5.0 x 10^{16} cm^{-2}
LPE HgCdTe SUBSTRATE
(111) RANDOM ORIENTATION
ROOM TEMPERATURE IMPLANTS
NO ANNEAL
150 keV
5.0 x 10^{16} cm^{-2}
^{1}H
^{2}H
300 keV
1.0 x 10^{16} cm^{-2}
^{1}H
^{2}H
HYDROGEN ATOM DENSITY, cm^{-3}
10^{22}
10^{21}
10^{20}
10^{19}
10^{18}
10^{17}
0
1
2
3
4
DEPTH, μm

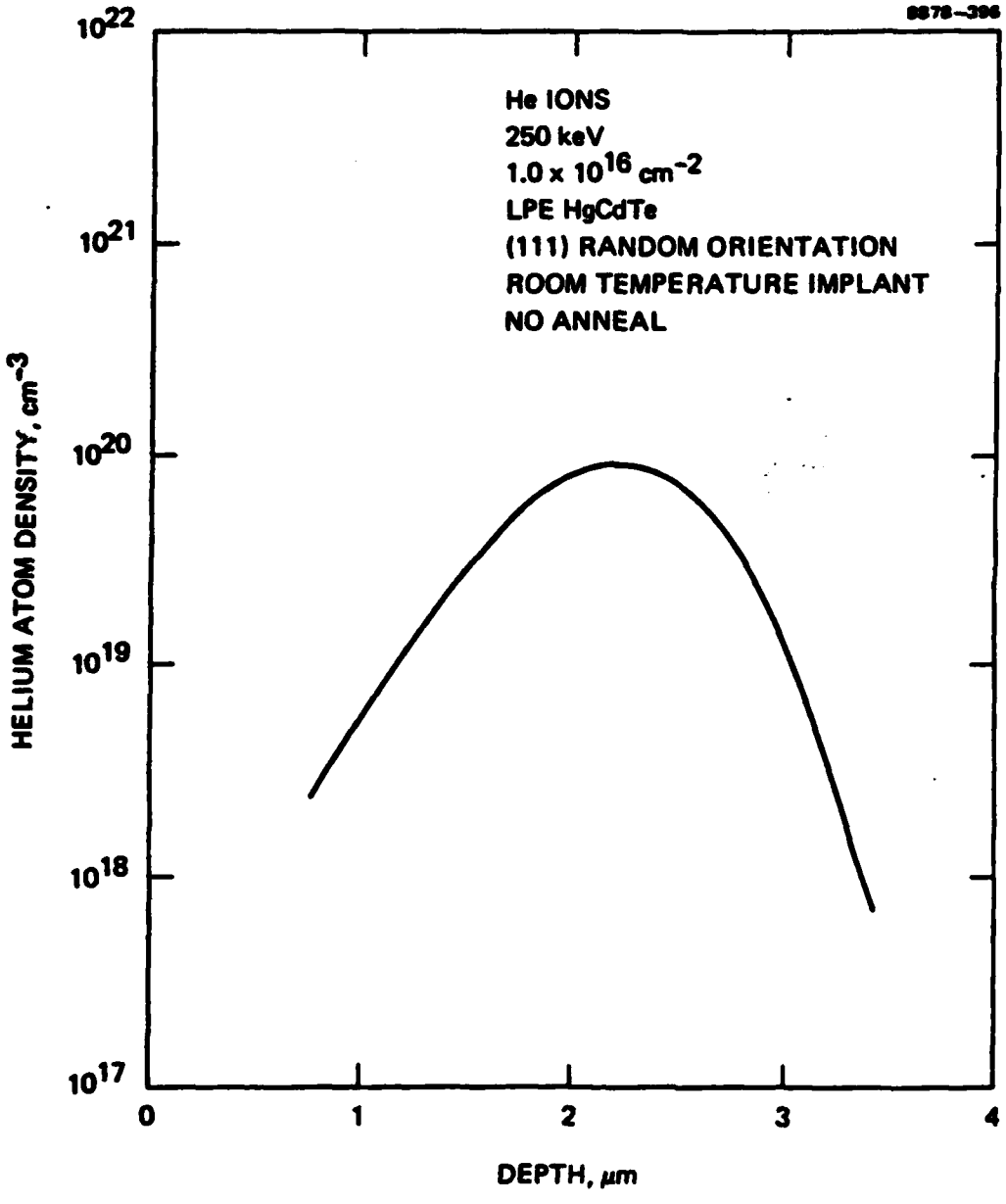
9878-396
He IONS
250 keV
1.0 x 10^16 cm^-2
LPE HgCdTe
(111) RANDOM ORIENTATION
ROOM TEMPERATURE IMPLANT
NO ANNEAL
HELIUM ATOM DENSITY, cm^-3
10^22
10^21
10^20
10^19
10^18
10^17
0
1
2
3
4
DEPTH, μm

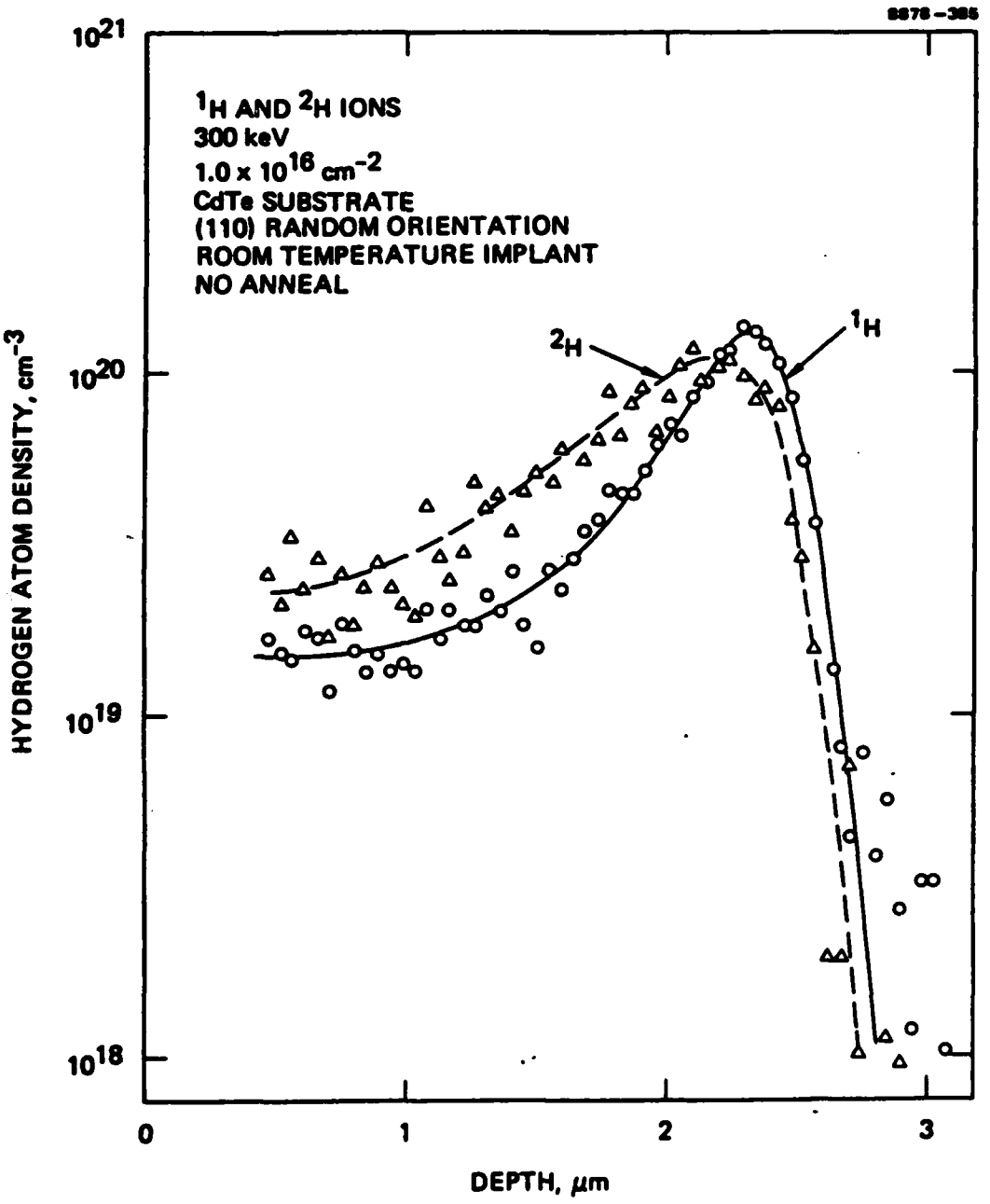
8878-385
^{1}H AND ^{2}H IONS
300 keV
1.0 x 10^{16} cm^{-2}
CdTe SUBSTRATE
(110) RANDOM ORIENTATION
ROOM TEMPERATURE IMPLANT
NO ANNEAL
^{2}H
^{1}H
HYDROGEN ATOM DENSITY, cm^{-3}
10^{21}
10^{20}
10^{19}
10^{18}
0
1
2
3
DEPTH, μm

Section III
Surface Study

Section III-1

The surface and interface properties of $Hg_{1-x}Cd_xTe$ cannot be understood without consideration of such conventionally bulk properties as the nature of the bonds which make up the lattice or the types and motion of extended defects in the material. The width of the liquid phase epitaxially grown (LPE) HgCdTe/CdTe heterojunction and accompanying broad distribution of dislocations[1] are examples of the way in which driving forces such as the difference in cation bonding[2] can affect what is normally considered interfacial behavior. The relationship between out-diffusion and evaporation of Hg from the surface to sample history or surface preparation[2] similarly indicates the need for a broadly based understanding in order to fully comprehend and solve surface and interface related problems.

This outlook is reflected in the work reported here. The electronic structure of the alloy at once accounts for the desired tunable bandgap of the materials as well as many materials problems in growth and preparation[2]. A detailed description of the electronic structure can be gained through the technique of angle-resolved photemission spectroscopy; a preliminary report on this project is the subject of Section III-2. Section III-3 presents results obtained using transmission electron microscopy to characterize extended defects observed at the LPE HgCdTe/CdTe heterojunction. This information is of value not only in characterizing an interface of extreme technological importance but also because analysis of the imaged defects can yield data on stacking fault energies and dislocation motion and annealing - data which strengthens the link between the bonding description originating in the electronic structure studies and macroscope materials properties.

To supplement the perspective gained from studies of the bonding, the surface properties were probed directly in a comparative study of activated oxygen uptake on the clean (110) faces of CdTe, HgTe, and $Hg_{0.69}Cd_{0.31}Te$ and in a first attempt at learning more about the mechanism of surface type conversion observed upon cleavage[3] by performing the cleaving at reduced temperature. These efforts are discussed in Sections III-4 and III-5 respectively. By an appropriate modification to the experimental procedure discussed in

Section III-4, initial data regarding the kinetics of the oxidation process were obtained which augment information on the chemistry of the oxygen-HgCdTe interaction. As pointed out in this section, both the chemical and kinetic trends can be understood in the framework of the alloy bonding.

References

1. T. J. Magee and G. R. Woolhouse, presented at U. S. Workshop on the Physics and Chemistry of HgCdTe, Dallas, TX, Feb. 8-10, 1983; Semiannual Report of this program, July 1, 1983.
2. W. E. Spicer, J. A. Silberman, I. Lindau, J. A. Wilson, A. Sher, and A.-B. Chen, J. Vac, Sci. Technol. A 1 (1983) 1735.
3. P. M. Raccah, U. Lee, J. A. Silberman, W. E. Spicer, and J. A. Wilson, Appl. Phys. Lett. 42 (9183) 374.

II. Angle-Resolved Photoemission Spectroscopy of $Hg_{1-x}Cd_xTe$: Preliminary Analysis of data from CdTe.

A) Introduction.

Once the electronic structure of a semiconductor is accurately known, properties ranging from the conduction band electron effective mass to the stacking fault energy can be estimated. In the case of Mercury Cadmium Telluride (MCT), the relationship between materials properties and electronic structure is particularly evident. Because of the higher nuclear charge of Hg compared to Cd, the selective penetration of the s-electron wave function to the nucleus, and the influence of the just completed d^{10} shell, the binding energy of the atomic Hg 6s valence electrons is 1.4 eV greater than that of the Cd 5s levels while the (unoccupied) valence p-orbitals have similar energies. This difference in the atomic valence states is central to the alloy electronic structure and is strikingly manifest in two aspects of the solid valence band structure when Hg and Cd are distributed in the cation sublattice of the MCT alloy.[1]

On the one hand, the states which comprise the conduction band minimum arise from the cation valence s-electrons; as Hg is substituted for Cd, the relativistic interactions of the high Z Hg core which are responsible for the increase in atomic s-electron ionization potential result in the decrease in fundamental bandgap of the alloy with increasing Hg content.[2] Thus the materials property which makes MCT attractive in practical applications, the ability to tune the optical absorption edge, is clearly a result of the unique electronic structure of the alloy.[1]

A second consequence of the atomic valence structure of Hg and Cd for the alloy electronic states relates to the bonding of Hg and Cd in the lattice.[1] In other semiconductor alloys studied to date,[3,4] the virtual crystal approximation (VCA) provides an adequate description of the alloy valence bands. In the VCA, use is made of a compositionally weighted average of the potentials of the distributed species -- Al and Ga in $Al_{1-x}Ga_xAs$, for example. This procedure allows one to treat the random

alloy with techniques applicable to a crystal with a periodic potential; however, it *a priori* renders the bonds between the various cations and anions indistinguishible. In the case of MCT, the difference in potential between Hg and Cd is sufficiently great that a description based the VCA fails for the cation s-electron derived states deep in the valence bands 3.5 to 6 eV below the valence band maximum.[5] It is clear that as a result of the distinct Hg or Cd contribution to the alloy electronic structure, the Hg-Te and Cd-Te bonds in MCT are different. The consequences of this bonding difference for properties such as dislocation formation and heterojunction growth[1] thus follow from the nature of the alloy valence electronic structure.

It should be noted that the breakdown of the VCA is selective in MCT.[5] As mentioned above, it occurs most strongly for the s-derived states deep in the valence bands. These states have k-values near the Brillouin zone boundary. At the zone center and the valence and conduction band edges, the VCA appears to be successful. The group of valence states with energy within about 3.5 eV of the valence band maximum (VBM) similarly exhibit behavior more nearly that expected in a periodic crystal or one in which the disorder in potential is small. (The states within 3.5 eV of the VBM have mainly Te p-electron character and are therefore less sensitive to the relativistic interactions which characterize the difference in Hg and Cd potintial.[5]) In order to fully characterize the selective breakdown of the VCA and thereby optimize the accuracy of calculations of the electronic structure and the materials properties that follow from knowledge of the electron states, a technique sensitive to both the electron energy and k vector in the solid is required. This sensitivity is provided by angle-resolved photoemission spectroscopy[7,8] (ARPES) in which both the photoemitted electron energy and angle of emission from the solid are determined.

B) Electron State selectivity of ARPES.

The electron states in a solid are characterized by the quantum numbers energy, E, and wave vector, k. In an ARPES experiment, electron emission induced by absorption of ultravialet light is collected in a small solid angle and in a specific direction relative to the crystal axes and energy

analyzed. The energy and wave vector of the free electron are thus determined. (The magnitude of the wave vector is fixed by the electron energy, and the direction is determined by the angular position of the detector.) The ability to relate these values outside the crystal and E and k for the states of the solid provides the utility of ARPES as a probe of the band structure of solids.

Photoemission can be viewed as a three step process (Figure 1).[9] Absorption of a photon produces an optical transition between two allowed states of the solid separated by the photon energy. If the excited electron has a velocity component in the direction of the surface, it may propagate toward the surface; the occurance of inelastic scattering during this step will remove electrons from the primary distribution. If the final state energy to which the electron was excited is sufficiently great, the electron has some probability of escaping the crystal once it reaches the surface. In the vacuum, the photoelectron's kinetic energy measured by the detector is referenced to the vacuum level. The valence band maximum serves as a convenient zero of energy in the crystal; hence, the measured kinetic energy and the final state energy in the photoabsorption event deffer by the sum of the semiconductor bandgap and electron affinity (see Figure 1). Because energy is conserved in the optical excitation process, the initial state lies $h\nu$ below the final state in energy. Thus, the measured photoelectron kinetic energy can be used to determine respectively the values E_f and E_i of the conduction band and valence band states involved.

When combined with conservation of energy, conservation of momentum in the optical excitation step of the photoemission process greatly restricts the number of possible transitions between valence and conduction band states in the solid. Figure 2 illustrates a reciprocal space representation of optical transitions between hypothetical initial and final state bands for two photon energies. In a categorization of the electron state wave vectors in which all k-values are reduced to the first Brillouin zone, conservation of momentum implies the initial and final states must have the same value of k. While the transition indicated by the solid arrow at k_1 which connects states of the same k value separated in energy by $h\nu_1$ may occur, the transition to the same final state from

the initial state at k_2 (dashed arrow labeled $h\nu_1$) satisfies energy conservation but not conservation of momentum and thus is not strictly allowed. The transition illustrated by the vertical arrow is refered to as a direct transition while the absolption from k equal k_2 is nondirect. Nondirect transitions do, in fact, occur[8], as will be evident in the data. As the photon energy is varied the optical excitation will occur from states at different E_i and k. (See $h\nu_2$ in Figure 2.) The variation in E_i and E_f with $h\nu$ will result in a shift in the kinetic energy of the photoelectron peak in the measured spectrum characteristic of the dispersion of the valence and conduction bands involved. In addition to conservation of energy and momentum, another constraint is imposed in the photoexcitation process. Selection rules determine for a given polarization which bands may participate in an optical transition based on the symmetry of the electron states which comprise the band and the direction of the optical electric field.[10] While k equal k_3 or k_4 is allowed for $h\nu_2$ in Figure 2, for example, the optical selection rules may exclude photoexcitation at k_4.

As discussed above, conservation of momentum in the excitation step ensures the equality of k_i and k_f. When the excited electron escapes over the surface potential barrier, a refraction phenomenon occurs such that only the component of k_f (and k_i) parallel to the surface plane is conserved.[7,8] Because the parallel component of the free electron wave vector outside the solid is determined by the angular position of the detector for a given electron energy, the choice of angle of detection similarly determines the value of k to which the experiment is sensitive inside the solid. The indeterminacy in the component of k_f perpendicular to the surface means that the valence and conduction band states which contribute to the ARPES spectrum lie along a line in reciprocal space given by k equal to a constant which depends on the electron energy. It is the ability to select the transitions occuring in the small volume of k-space along this line out of all possible allowed transitons that makes ARPES such a sensitive probe of electronic structure.

C) Experimental

The ambiguity in determining the value of k when only $k_{||}$ is known can be

overcome by careful analysis of the photoemission data, as discussed below (section D). Such analysis is simplified for particular choices of k. Positioning of the detector along the normal to the sample surface ensures that the states contributing to the measured energy distribution lie in the direction of k-space normal to the plane of the surface. In the data reported, the (110) face of $Hg_{1-x}Cd_xTe$ (x=1.0, 0.31, 0.23, and 0.0) was prepared by cleaving in vacuum, and data was collected in the normal emission geometry. Thus the measurements are sensitive to valence and conduction band states in the (110) direction or $\Gamma\Sigma KSX$ symmetry axis of the Brillouin zone (Figure 3). Additional measurements were made with k_i chosen to lie on the hexagonal face of the Brillouin zone (WLW in Figure 3) for initial states of high s-character 4.6 to 6 eV below the VBM in order to explore the breakdown of the VCA for states at the zone boundary. This data will appear in a future report. Spectra were recorded for photon energies between 13 and 27 eV using the 8 degree beam line at the Stanford Synchrotron Radiation Laboratory. By varying the angle of incidence of the photon beam between 20 and 64 degrees, the polarization could be similarly altered. The component of the electric field vector in the plane of the surface was parallel to the $(i\bar{1}0)$ direction.

D) Results and Method of Analysis for CdTe.

Analysis of the spectra from HgTe and the alloy samples is continuing. While the analysis of the CdTe data is not yet in its final form, sufficient progress has been made to demonstrate the ARPES technique for band structure determination. Normal emission data as a function of photon energy from (110) CdTe for 20 degree (stronger s polarization) and 64 (stronger p polarization) angles of incidence are presented in Figures 4 and 5 respectively. Both sets of spectra exhibit similar structure which generally disperses as the photon energy is varied, indication origin in bulk rather than surface states. Increasing the p polarization content of the incident beam enhances the structures which for $h\nu$=18 eV occur near -4.6, -3.6, and -1.2 eV, sometimes obscuring weaker peaks. The increase in strength of these peaks indicates a Σ_1 character.[10]

While the use of normal emission restricts the region of k-space contributing to the photoemission to the Σ axis, the exact locations along

this line where the transitions occur must be determined by analysis. The criteria to be met by the proper assignment of the structure in the spectra to parts of the Brillouin zone include the correct measured final state energy, E_f, and the correct spearation between E_f and E_i such that final and initial states lie on the conduction and valence bands at the same value of k. One approach[11] succesfully employed in other cases assumes a free electron parabola for the final state with energy origin V_0 below the VBM; from the relation

$$E_f = \hbar^2k^2/2m - V_0$$

one can determine k and E_i and thereby map the valence bands. When an accurate initial state band structure is known, a reverse proceedure can be used to determine the high lying conduction band final states.[12,13] In this case E_i is determined from the photoemission spectra by first locating the position of the VBM in the data. From the band structure, one can then find the value of k (there may, in fact, be more than one) corresponding to E_i for a given peak in the spectrum and photon energy and then locate E_f at this value of k.

Band structure calculations for the initial statees in CdTe in the (110) direction have been published.[14,15] These calculations do not include conduction bands with high enough energy for direct comparison to the data. The analytical approach adopted was to <u>assume</u> the nonlocal pseudopotential calculation of Chelikowsky and Cohen (reference 14) to be correct, determine all possible k_i corresponding to a photoemission peak at E_i, and hence locate candidate final states at each k_i. A choice of a particular k from the set of possible wave vectors was then made by comparing the candidate $E_f(k_i)$ with the set of free electron parabolas of the face centered cubic lattice.

The selected final states and free electron parabolas are shown in Figure 6. In most cases, the final states are found to lie near the segment of free electron parabola which was translated into the first Brillouin zone by reciprocal lattice vector (110)$4\pi/a$ and is thus part of the parabola centered at Γ. It should thus be the major contributor to the photoemission process,[11] as was indeed found. The group of final states rising in energy near k equal 0.85 are due to transitions arising from the

high density of states region with initial state energy of approximately -4.6 eV. While the intensity of emission in this peak is stronger when a final state band is available, the transitions nonetheless occur for all photon energies. This is an example of a nondirect transition;[8] provided the initial states lie along Σ, the absence of other bands at this binding energy allows assignment of the structure to the lowest valence band. (See Figure 7).

To obtain agreement between the measured final states and the free electron bands, a value of inner potential, V_0, of 4.3 eV was required. This choice of V_0 is consistent with that obtained from analysis of the Low Energy Electron Diffraction (LEED) intensity profiles by Duke *et al*[16], who determined a value of 4 eV. (In GaAs, the ARPES value of 9.32 eV is to be compared to 8 eV from LEED data.[11]) The initial states contributing to the spectrum based on this preliminary analysis are shown in Figure 7.

E) Future Analysis

To examine the accuracy of band structure calculations, a better representation of the final state bands is needed. The reasonable agreement with the free electron bands indicates that it may be possible to calculate the true conduction band structure with merely small perturbations to the free electron parabolas. Analysis of the data for the alloys must also be performed. The similarity in the emission from these compounds should aid in establishing a consistent assignment of the peaks. Little use of the polarization dependence of the spectra has been made so far, and this information will likewise give confidence to the electronic structure determination. Finally, the aspect of the electronic structure of MCT key to understanding the alloy bonding properties is the selective breakdown of the VCA; examination of the composition dependence of the width of emission from the s-electron derived valence states near the zone boundary should provide information on parameters unique to non-VCA calculations[17,18] of the alloy electronic structure.

References

1. W.E. Spicer, J.A. Silberman, I. Lindau, A.-B. Chen, A. Sher, and J.A. Wilson, J. Vac. Sci. Technol. A 1 (1983) 1735

2. A. Kisiel and P.M. Lee, J. Phys. F 2 (1972) 395.

3. D. Stroud and H.ehrenreich, Phys. Rev. B 2 (1970) 3197.

4. A.-B. Chen and A. Sher, Phys. Rev. B 10 (1981) 948.

5. W.E. Spicer, J.A. Silberman, P. Morgen, I. Lindau, J.A. Wilson, A.-B. Chen, and A. Sher, Phys. Rev. Lett. 49 (1982) 948.

6. W.E. Spicer, J.A. Silberman, I. Lindau, A.-B. Chen, A. Sher, and J.A. Wilson, J. Vac. Sci. Technol. A 1 (1983) 1735.

7. E.W. Plummer and W. Eberhardt, in Advances in Chemistry, 49 (1982) 533.

8. F.J. Himpsil, in Advances in Physics, 32 (1983) 1.

9. W.E. Spicer, in Optical Properties of Solids -- New Developments, ed. by B.O. Seraphin, North Holland Publishing Co. (Amsterdam, 1976).

10. W. Eberhardt and F.J. Himpsel, Phys. Rev. B 21 (1980) 5572.

11. T.C. Chang, J.A. Knapp, M. Aono, and D.E. Eastman, Phys. Rev. B 21 (1980) 3513.

12. K.A. Mills, D. Denley, P. Perfetti, and D.A. Shirley, Solid State Comm. 30 (1979) 743.

13. J.G. Nelson, W.J. Gignac, R.S. Williams, S.W. Robey, J.G. Tobin, and D.A. Shirley, Surf. Sci. 131 (1983) 290.

14. James R. Chelikowsky and Marvin L. Cohen, Phys. Rev. B 14 (1976) 556.

15. Shin-ichi Katsuki and Makoto Kunimune, J. Phys. Soc. Japan 31 (1971) 415.

16. C.B. Duke, A. Paton, W.K. Ford, A. Kahn, and G. Scott, Phys. Rev. B 24 (1981) 3310.

17. An-Ban Chen and A. Sher, J. Vac. Sci. Technol. 21 (1982) 138.

18. K.C. Hass, H. Ehrenreich, and B. Velicky, Phys. Rev. B 27 (1983) 1088.

Figure Captions

Figure 1. Schematic description of photoemission as a three step process involving photoexcitation, transport of the excited electron distribution to the surface, and escape into the vacuum.

Figure 2. Reciprocal space representation of photoexcitation step illustrating constraints on k and E imposed by conservation of energy and momentum. (See text.)

Figure 3. First Brillouin zone for a face centered cubic crystal. The lines probed in the reported ARPES experiment are shown dashed.

Figure 4. Normal emission energy distribution curves from (110) CdTe plotted against initial state energy (relative to the valence band maximum). The spectra were recorded for $13 \leq h\nu \leq 26$ eV in 0.5 eV steps for polarization 20 degrees from the surface and along the (110) direction.

Figure 5. Same as Figure 4 but with the polarization vector 64 degrees from the surface along the (110) direction.

Figure 6. Free electron parabolas for the body centered cubic recciprocal lattice along Σ. The solid curves are the parts of the free electron final state parabola centered at the origin and should be the strongest contributor to the photoemission. The points represent measured final states if the initial bands of Chelikowsky and Cohen[14] are assumed.

Figure 7. Initial state bands of Ref. 14 and location of structure observed in the ARPES. The structure was assumed to match the band calculation in order to map the final states. (See text.)

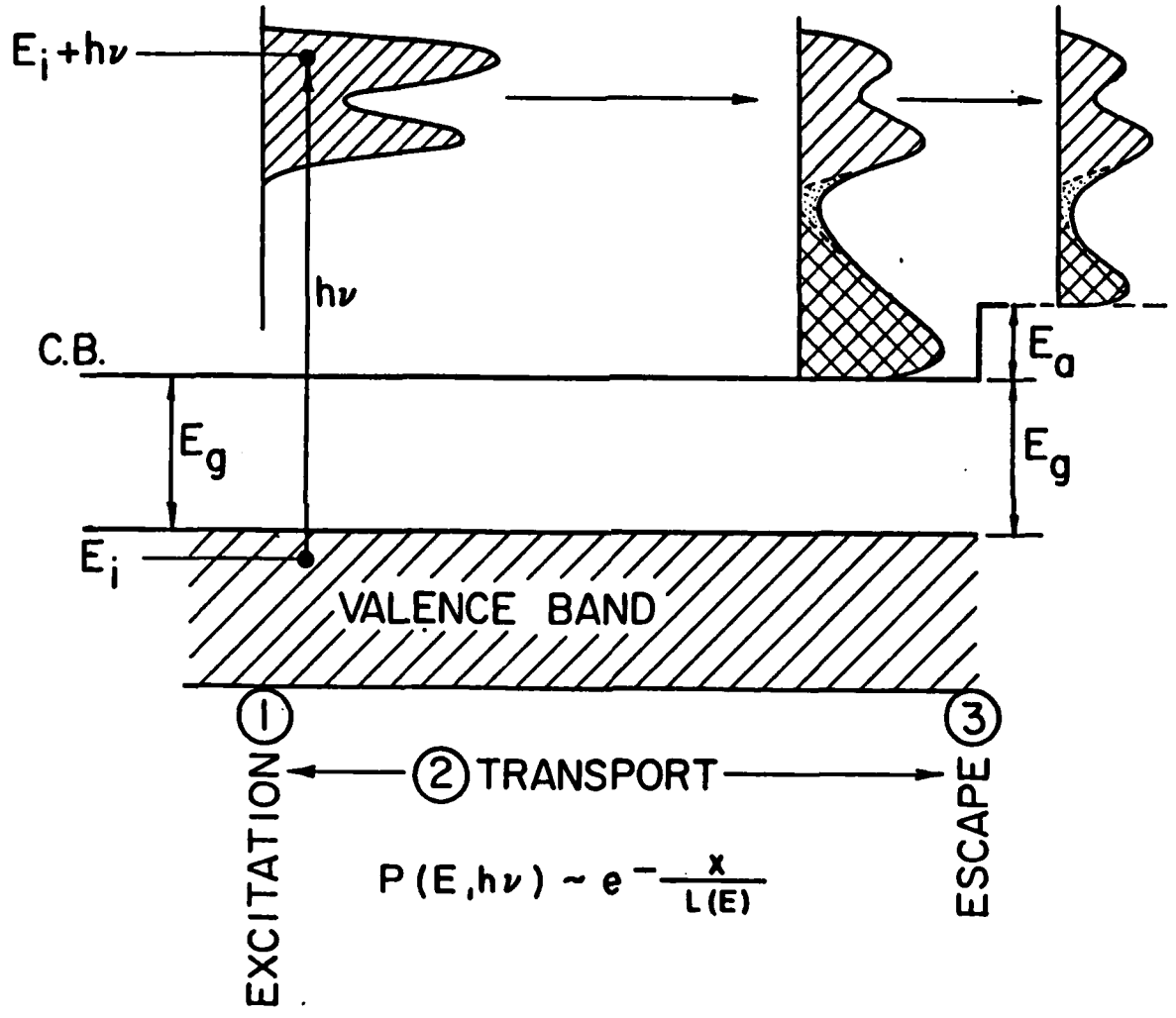
$E_i + h\nu$
$h\nu$
C.B.
E_a
E_g
E_g
E_i
VALENCE BAND
EXCITATION (1)
(2) TRANSPORT
ESCAPE (3)
$P(E, h\nu) \sim e^{-\frac{x}{L(E)}}$

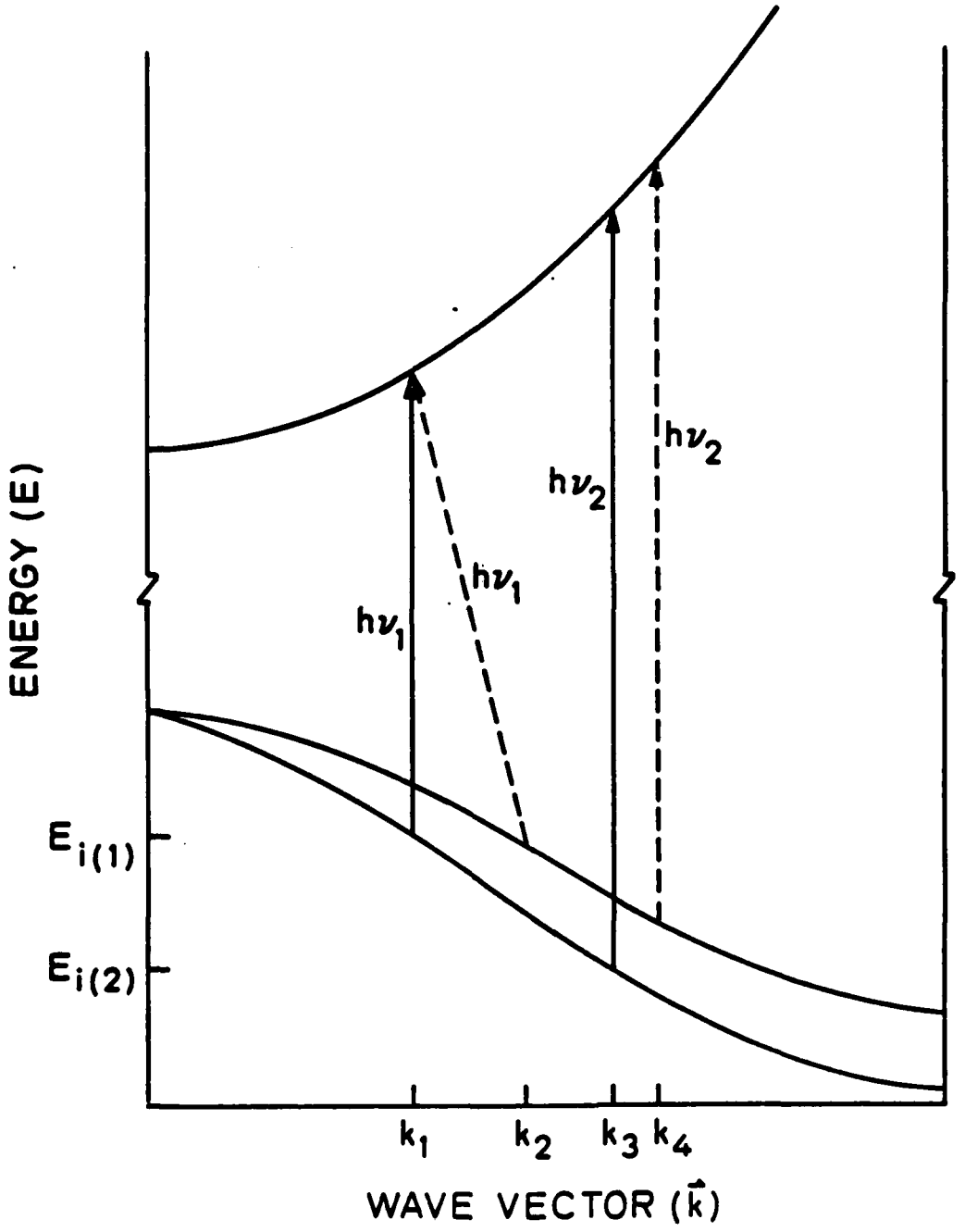
ENERGY (E)
$h\nu_1$
$h\nu_1$
$h\nu_2$
$h\nu_2$
$E_{i(1)}$
$E_{i(2)}$
k_1
k_2
k_3
k_4
WAVE VECTOR ($\vec{k}$)

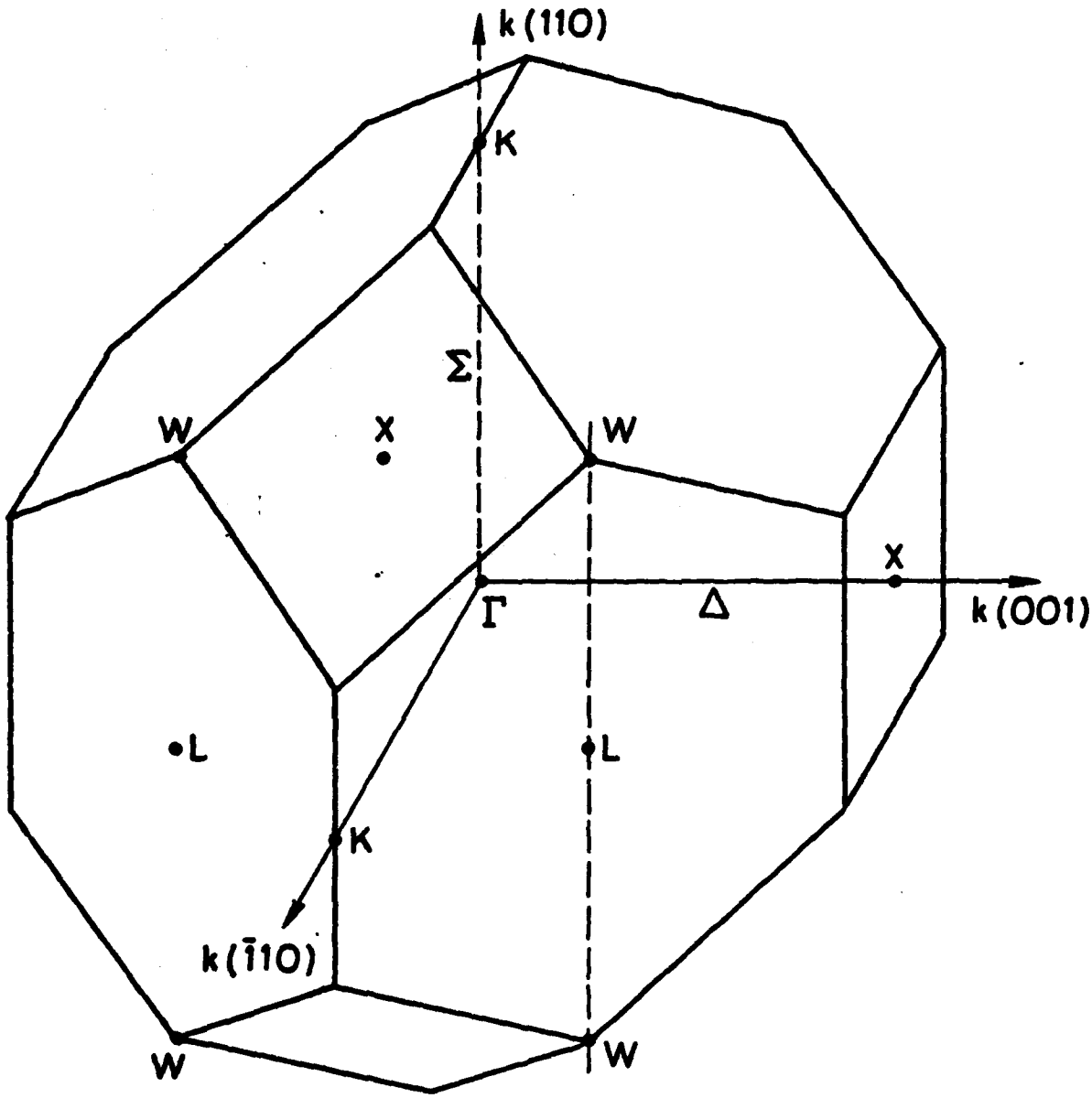
k (110)
K
Σ
W
X
W
X
Γ
Δ
k (001)
L
L
K
k (1̄10)
W
W

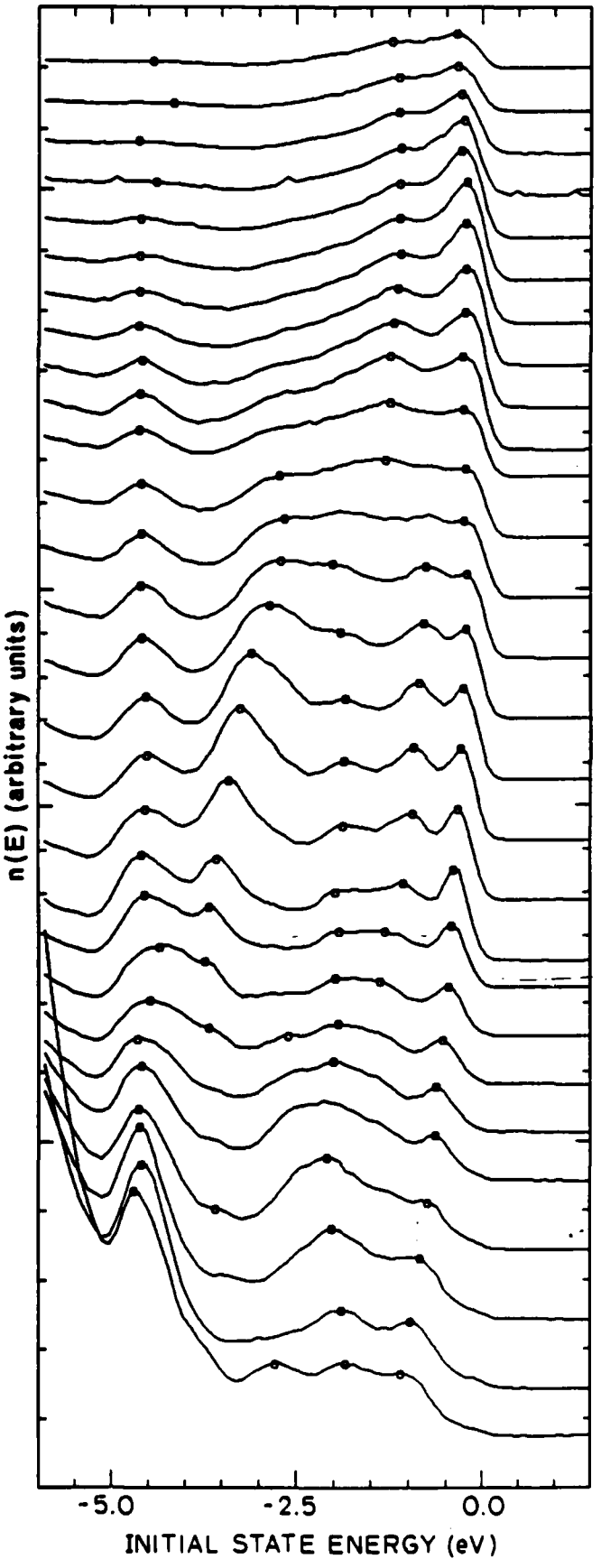
n(E) (arbitrary units)
-5.0
-2.5
0.0
INITIAL STATE ENERGY (eV)

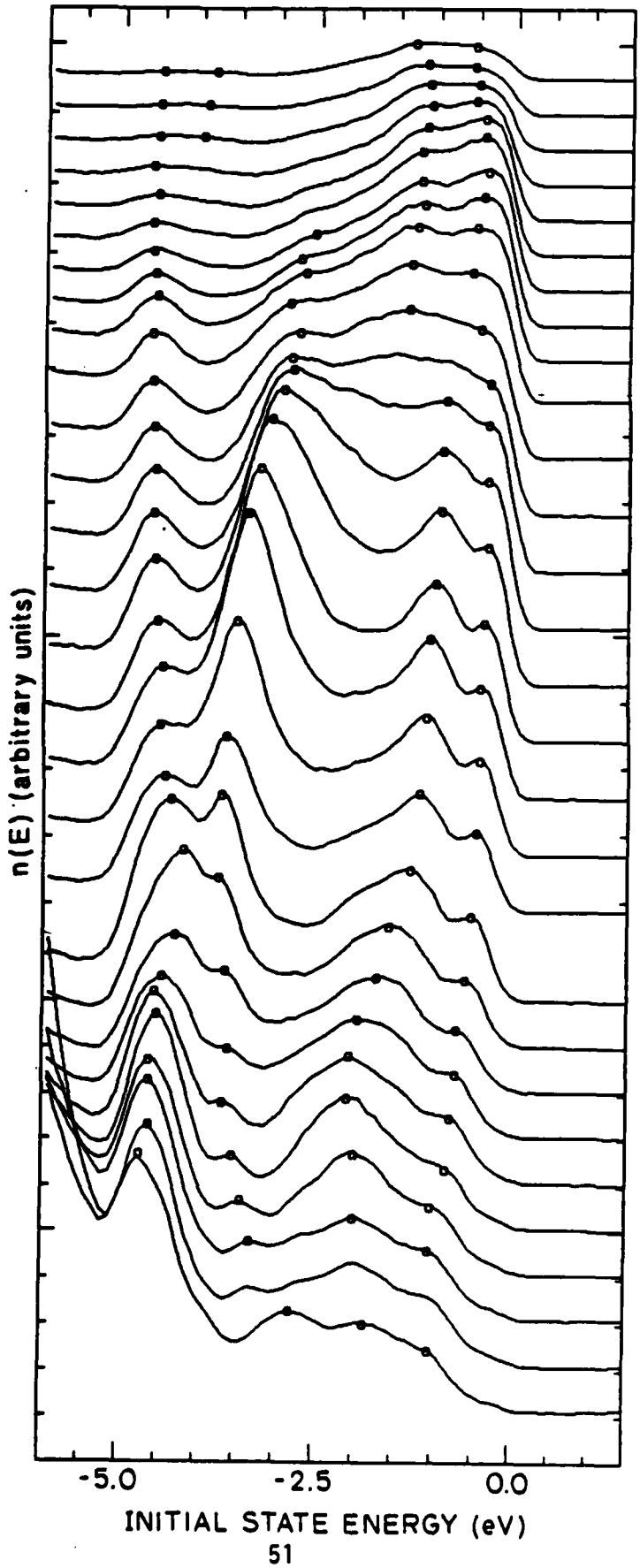
n(E) (arbitrary units)
-5.0
-2.5
0.0
INITIAL STATE ENERGY (eV)

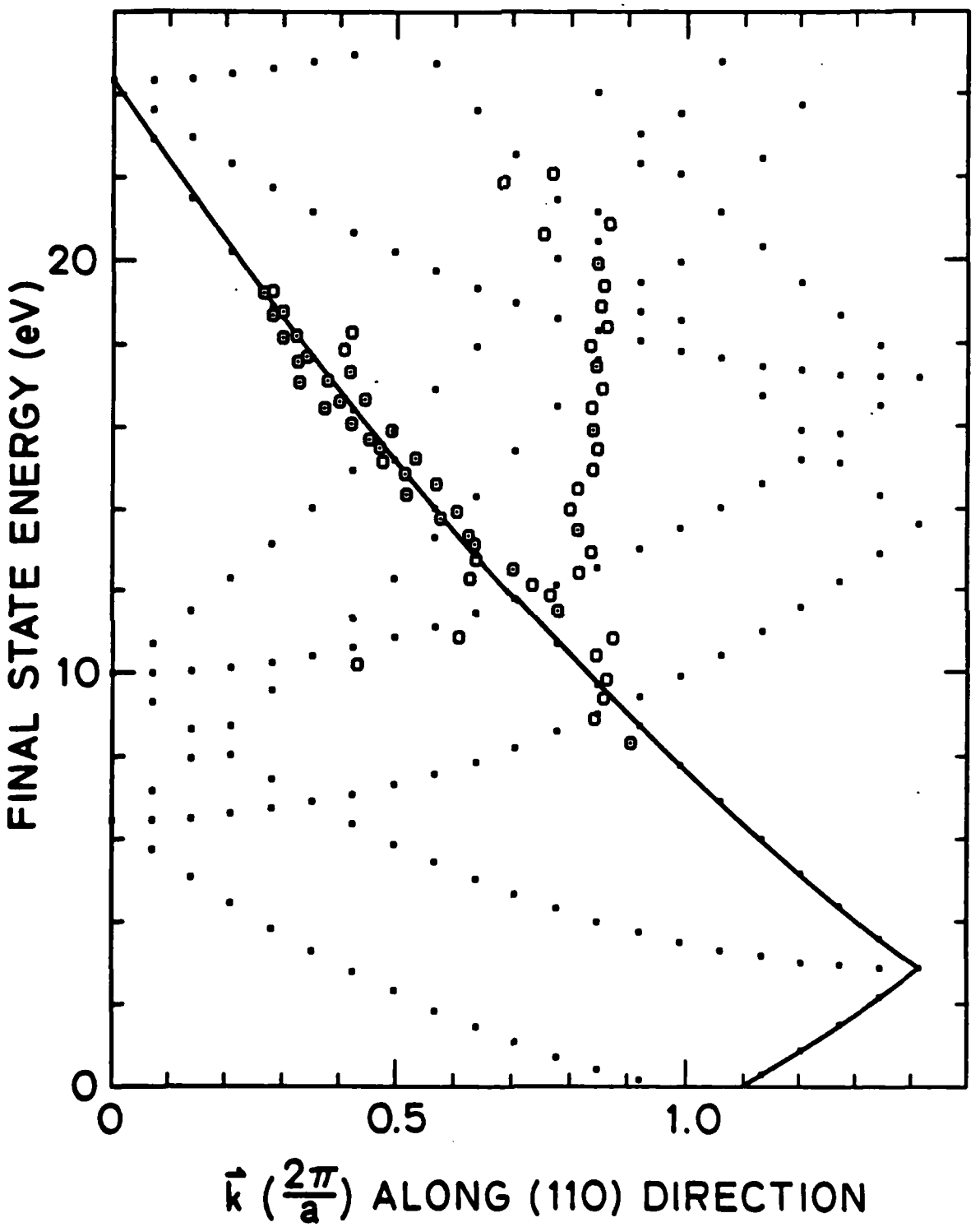
FINAL STATE ENERGY (eV)
20
10
0
0
0.5
1.0
$\vec{k}$ ($\frac{2\pi}{a}$) ALONG (110) DIRECTION

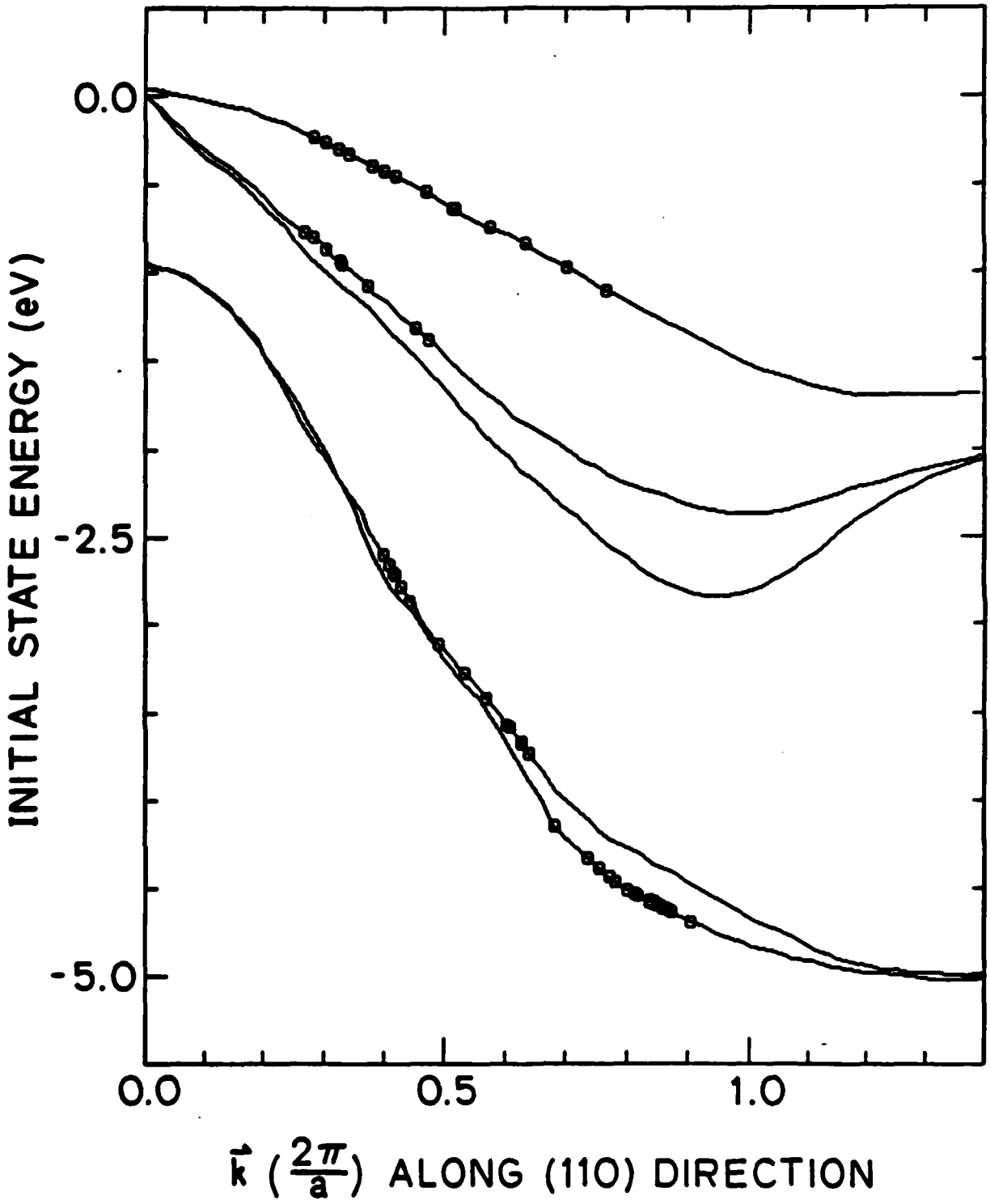
0.0
-2.5
-5.0
INITIAL STATE ENERGY (eV)
0.0
0.5
1.0
$\vec{k}$ ($\frac{2\pi}{a}$) ALONG (110) DIRECTION

Section III-3

TEM STUDIES OF DEFECTS

Detailed defect structural characterization of MCT has been established as an essential prerequisite to understanding and improving this material. The p- to n-type conversion upon mechanical damage [1-3] or ion implantation, width of the LPE grown MCT on CdTe heterojunction [4], and Hg out-diffusion after mechanical damage [5] are a few of the observed phenomena in MCT that link the mechanical defect structure with the electronic structure. Transmission Electron Microscopy (TEM) is probably one of the most useful techniques in viewing directly the defect microstructure associated with these phenomena, and has been employed here with the primary focus on the LPE grown heterojunction and the mechanical damage resulting from ion milling. The damage induced by ion milling is believed to be similar to that introduced by ion implantation.

In order to gain insight into the defect structure associated with the liquid phase epitaxy (LPE) grown MCT on CdTe interface, TEM samples have been prepared for view in cross-section. Because it is of great interest to view the defect distribution as a function of distance from the metallurgical junction, cross-sectional TEM samples were prepared since it is possible to view this profile directly in only one successfully prepared sample. The heterojunction studied was a LPE grown MCT ($x = 0.3$) on a (111) CdTe substrate supplied by SBRC. This LPE material was grown from a Te melt to a layer thickness of 15.8 μ m.

The samples were prepared by cutting two adjacent 1.0 x 1.5 mm rectangular pieces from the LPE substrate and cementing them together so that the LPE MCT layers were sandwiched between the CdTe substrates. Care was taken to insure that the (110) plane was oriented parallel to one of the sample edges, so that lattice images could be taken if the preparation of the sample was successful. This resulting "sandwich" was then imbedded in Bakelight, which acts as a

supporting material when the sample is very thin. The samples were then mechanically thinned to a thickness of approximately 150 μ m, and then dimpled so that approximately 10 μ m of material was left in the center cross-section of the sample. The final thinning step employed ion milling where the sample was milled at room temperature until perforation occurred. In light of the ease of introducing artifacts into MCT because of its ease of mechanical deformation even at room temperature [6], it is to be emphasized here that this sample preparation technique was attempted because of its previous success on CdTe, not because it has been shown to be successful on MCT. Indeed, our previous experiences with ion milling showed that this thinning technique does introduce defects.

The ion milling employed in final thinning step is indeed seen to introduce large densities of defects. The results of this preparation technique are shown in Figure 1. Conventional 2 - beam imaging at the low magnification of the interfacial region reveals a defect density that is very much higher (2 to 3 orders of magnitude) in the CdTe than in the MCT. Figures 1a, b, and c are micrographs illustrating this effect. These are taken from the interface region, away from the interface on the MCT side, and away from the interface on the CdTe side, respectively. The defects in the CdTe appear to consist of dense tangles of dislocations and large numbers of small loops. The defect density decreases over several microns from the heterojunction into the MCT where the defects are predominantly single-line dislocations with occasional large loops. Since this density of defects is extremely high, it is seen that this current preparation technique is rendered prohibitive in studying the original defect structure associated with the heterojunction since it causes damage that completely masks this original defect structure.

However, since the MCT and the CdTe have been ion milled under identical conditions in this technique, a direct comparison of the ion bombared induced defects between the MCT and CdTe can be undertaken. In addition, the MCT-CdTe heterojunction can be examined. It is therefore possible to extract important information of the defect energetics from these ion-damaged cross-sectional samples.

Additional insight into the nature of these ion-induced defects is obtained if higher magnifications are used in studying the defects. Lattice images (to our knowledge, these are the first such images obtained from HgCdTe) of the heterojunction region reveal a much higher density of dissociated 60° dislocations and interstitial loops in the CdTe than in the MCT consistent with the above observations on their density. This high density is commonly observed in ion-milled CdTe [7]. Typical results are shown in Figure 2. Figure 2a shows a lattice image of a representative area in the CdTe side of the heterojunction where many extrinsic stacking faults (ESF) are readily observed. That there exist a much lower density of defects in the MCT side of the heterojunction can be seen in Figure 2b, where a representative area contains no defects at all. Figure 2c shows an almost perfect 60° in the MCT, where the arrow is pointing down the extra half-plane. To the best of our knowledge, perfect 60° dislocation have not been observed in CdTe. Figure 2d shows a typical ESF in the MCT, with the width between the two Shockley partial dislocations always observed to be less in this material than in CdTe.

That there is a much lower defect density in the HgCdTe than in the CdTe when damages under the same milling conditions at first seems surprising. Cole has shown that HgCdTe is easily deformable even at room temperature, which produced large densities of dislocations [6]. Cole also showed that the rate of glide of dislocations is similar in the two materials because the room

temperature hardness of CdTe and MCT (x = 0.3) are similar. In light of this information, intuition leads us to expect that just as many or more defects will be present in the MCT side of this ion-milled heterojunction. That this is not the case suggests that the defect energetics are different for the two materials, and that some recovery mechanism exists in the MCT, the rate of which being much more rapid in this material than in CdTe. The differences in the defect densities on either side of the heterojunction cannot be attributed to differences in the glide behavior since the hardness numbers are similar, therefore other recovery mechanisms must be occurring. This in agreement with theoretical calculations of Harrison [8].

Insight into the difference of recovery rate for these two materials can be gained from these results. The information obtained from the lattice images taken from both of these regions reveal that there is a small dissociation of the Shockley partial dislocations in the MCT relative to the CdTe, which suggests that the climb of dislocations in MCT is much easier than in the CdTe. Dislocation climb is a diffusion-controlled process with vacancies diffusing to the dislocation core as the rate determining step. The narrower stacking fault has fewer atomic sites to which vacancies must diffust to cause it to climb, hence this process should be more rapid in the MCT with its correspondingly narrow ESF. This might also be aided by a large density of point defects in ion bombarded MCT, arising from the weak Hg-Te bond and the consequent ease of formation of the Hg vacancy [8,9].

Since the nature of the damage introduced by ion milling is similar to that of ion implantation damage, TEM lattice imaging could be used to study the nature of these ion-implantation defects. Thus, lattice imaging might find suitable applications in understanding some of the critical technological problems associated with ion implantation damage to the MCT lattice

as well as those involved in LPE growth of MCT on CdTe. In the case of studying heterojunctions in cross section, methods to thin the material without introducing artifacts must be developed in order to study the original defect structure. These studies are currently under investigation.

References

1. R. R. Daniels, G. Margaritondo, G. D. Davis, and N. E. Byer, Appl. Phys. Lett. 42, 50 (1983).
2. G. D. Davis, N. E Byer, R. R. Daniels, and G. Maryaritondo, J. Vac. Sci. Technol. A 1, 1726 (1983).
3. P. M. Raccah, U. Lee, J. A. Silberman, W. E. Spicer, and J. A. Wilson, Appl. Phys. Lett. 42, 374 (1983).
4. G. R. Woolhouse, H. Kawayoski, and T. J. Magee, paper presented at AACG, 6th Conference on Crystal Growth, Fallen Leaf Lake (1982).
5. H. M. Nitz, O. Ganschow, U. Kaiser, L. Wiedmann, and A. Benninghoven, Surf. Sci. 104, 365 (1982).
6. S. Cole, M. Brown, and A. W. F. Willoughby, J. Mater. Sci. 17, 2061 (1982).
7. T. Yamashita, private communication.
8. W. A. Harrison, J. Vac. Sci. Technol. A 1, 1672 (1983).
9. W. E. Spicer, J. A. Silberman, I. Lindau, A.-B. Chen, A. Sher, and J. A. Wilson, J. Vac. Sci. Technol. A 1, 1735 (1983).

Figure Captions

Figure 1a: Conventional 2-beam TEM micrograph of the ion-milled HgCdTe-CdTe heterojunction showing the defect structure of this damaged region.

Figure 1b: In the HgCdTe away from the heterojunction showing lower density of defects.

Figure 1c: In the CdTe side of the heterojunction showing 2-3 orders of magnitude higher density of defects.

Figure 2a: TEM lattice image on the CdTe side of the heterojunction. This representative area is seen to possess a high density of extrinsic stacking faults (ESF).

Figure 2b: Lattice image taken from a representative area on the HgCdTe side of the heterojunction showing no defects.

Figure 2c: Lattic image showing an almost perfect 60° edge dislocation in the HgCdTe side of the heterojunction. The arrow points down the extra half-plane.

Figure 2d: Dissociated dislocation in the HgCdTe. Notice the much narrower extrinsic stacking fault (ESF) width in this material as compared to the CdTe ESF width.

Section III-4

Activated Oxygen Uptake on HgTe, CdTe, and $Hg_{0.69}Cd_{0.31}Te$[a]

J. A. Silberman[b], D. Laser[c], I. Lindau, and W. E. Spicer[d]

Stanford Electronics Laboratory
Stanford University
Stanford, CA 94305

J. A. Wilson

Santa Barbara Research Center, Goleta, CA 93017

A study of the oxidation of the semiconductor alloy $Hg_{1-x}Cd_xTe$ can afford insights into the surface chemistry of the alloy and the way in which the properties of the constituents (eg. HgTe and CdTe) are modified by alloy formation. From experimental [1] as well as theoretical [2] investigation of the alloy electronic structure it is known that the cation s-electron derived contribution to the deep valence states in $Hg_{1-x}Cd_xTe$ reflect distinct Hg or Cd origin rather than indicate a single average or virtual cation. The separate contribution to the valence electronic structure by the cations implies a difference in the bonding of Hg and Cd to Te. The more metallic nature of the HgTe bond reduces the bond strength in HgTe compared to CdTe [3], and the observation of binding energy shifts in the Cd 4d and Hg 5d levels in $Hg_{1-x}Cd_xTe$ compared to the binary compounds suggests the disparity in bond strength increases upon alloy formation [1]. In a comparative study of oxygen uptake on CdTe, HgTe, and $Hg_{0.69}Cd_{0.31}Te$ discussed below, the modification of the Cd-Te bonding properties are manifest in a decrease in activity of this site in the alloy compared to CdTe, and the weaker Hg-Te bond is observed to play a rate determining role in the alloy oxide formation.

To examine the oxidation chemistry of these compounds, photoemission spectroscopy using synchrotron radiation was used to monitor the effects of oxygen exposure on the surfaces of (110) oriented HgTe, CdTe and

$Hg_{0.69}Cd_{0.31}Te$ cleaved in vacuum. Because these compounds are highly inert to oxygen in the molecular ground state [4], uptake was stimulated by a hot filament positioned in line-of-sight of the sample face. So that a linear exposure scale could be established, each sample was exposed to multiples of a fixed dose (5×10^{-5} torr of O_2 for 500 sec) thereby allowing comparison of the rate of oxidation. The photoemission spectra of the valence band, Hg 5d, and Cd 4d core levels (Figure 1) and the Te 4d core lines (Figure 2) following each exposure document the interaction of oxygen activated by the line-of-sight hot filament with $Hg_{1-x}Cd_xTe$. Oxygen accumulates with each exposure, as evidenced by the increase of O 2p derived emission at about 46 eV (Figure 1). A second oxygen induced structure occurs near 42.2 eV and overlaps the Hg $5d_{5/2}$ line; this second feature is readily observed in the case of CdTe. The binding energy of the main O 2p structure relative to the valence band maximum increases by roughly 0.5 eV in HgTe compared to CdTe. In addition to growth of the oxygen related structure, exposure to activated oxygen results in attenuation of the Hg 5d core levels. (Because of the substantial overlap of the Hg $5d_{5/2}$ peak with the oxygen derived structure, this is best followed with the Hg $5d_{3/2}$ line.) The Cd emission, on the other hand, slightly strengthens, indicating that while Hg is released upon oxygen uptake, Cd is retained in the oxide. Release of Hg is observed in the initial stages of HgTe oxidation as well.

Oxide formation is signalled from the initial exposure by the appearance of Te 4d emission approximately 3.6 eV more tightly bound (Figure 2) which increases in magnitude with additional exposure. With each dose, the Te signal at the clean surface position is attenuated by the growing oxide film. That the Te in the alloy and Hg signals diminish

at the same rate suggests Hg is released as a consequence of or as a step in the oxidation process at the initial stages studied here. In addition to the oxidized and lattice bound Te, a third state of Te results from the first exposure. Emission from 4d states 0.6 eV more tightly bound than in the bulk produces the asymmetric broadening of the core level emission near the bulk Te position seen in the spectra (Figure 2). The binding energy of this third contribution to the Te emission indicates elemental Te [5] is produced by the exposure and probably results from a loss of Hg in excess of the quantity of oxide formed during the first dose. The extent to which this occurs varies from surface to surface and may depend on the number of imperfections produced upon cleavage.

Examination of the rate of oxygen uptake by the three materials may provide further information as to the reactions controlling oxide growth. From the ratio of oxidized to unoxidized Te peaks in the spectra for each sample and after suitable correction for the inelastic mean free path of the photoemitted electron (assumed constant), the thickness of the oxide film can be determined as a function of the number of standard exposures for the three compounds. This data is given in Figure 3. Several observations regarding the relative rates relate to the oxidation process. In every case the oxide grows in proportion to the exposure. In the available data, there is no evidence of saturation for films grown in excess of at least two monolayers. The rate of oxide production for the alloy is 69% as great as that of the binary HgTe; i.e., the rate of growth scales with the number of HgTe bonds. This observation is consistent with the correlation of the release of Hg and oxide formation noted in the core level spectra. Finally, that the alloy of this composition oxidized more slowly than CdTe implies reduced activity at the Cd-Te

sites in the alloy. The rate limiting role of the weaker Hg-Te bond as well as the modified interactions of the Cd-Te sites are consistent with the changes in electronic structure between HgTe, CdTe, and the ternary; studies of additional compositions as well as identification of the nature of the desorbing Hg will provide further insights into the oxidation reaction and thus detail the relation of the surface electronic structure and oxygen chemistry.

a) supported by DARPA contract No. 916610-B2. Work performed at the Stanford Synchtrotron Radiation Laboratory which is supported by the Department of Energy, Office of Basic Energy Sciences and the National Science Foundation, Division of Materials Research.
b) Fannie and John Hertz Foundation Fellow
c) Permanent address: Ministry of Defense, Box 2250, Haifa, Israel
d) Stanford Ascherman Professor of Electrical Engineering.

References

1. J. A. Silberman, P. Morgan, I. Lindau, W. E. Spicer, and J. A. Wilson, J. Vac. Sci. Technol., 21, (1982) 142.

2. A-B. Chen and A. Sher, J. Vac. Sci. Technol., 21, (1982) 138; K. C. Hass, H. Ehrenreich, and B. Velicky, Phys. Rev. B, 27 (1983) 1088.

3. W. A. Harrison, J. Vac. Sci. Technol., A1 (1983) 1672.

4. P. Morgen, J. A. Silberman, I. Lindau, W. E. Spicer, and J. A. Wilson J. Electr. Mater., 11, (1982) 597.

5. David R. Rhiger and Robert E. Kvass, J. Vac. Sci. Technol., 21 (1982) 448.

Figure Captions

Figure 1. Photoemission spectra from the valence band, Hg 5d (40.5 and 42.3 eV), and Cd 4d (centered around 39.5 eV) core levels for the clean surface and following each oxygen dose. The valence band maximum is located at 50.2 eV.

Figure 2. Photoemission spectra of the Te 4d core lines for the clean surface and with increasing oxygen exposure.

Figure 3. Thickness of the oxide film measured in multiples of the electron inelastic mean free path versus exposure in multiples of a standard dose.

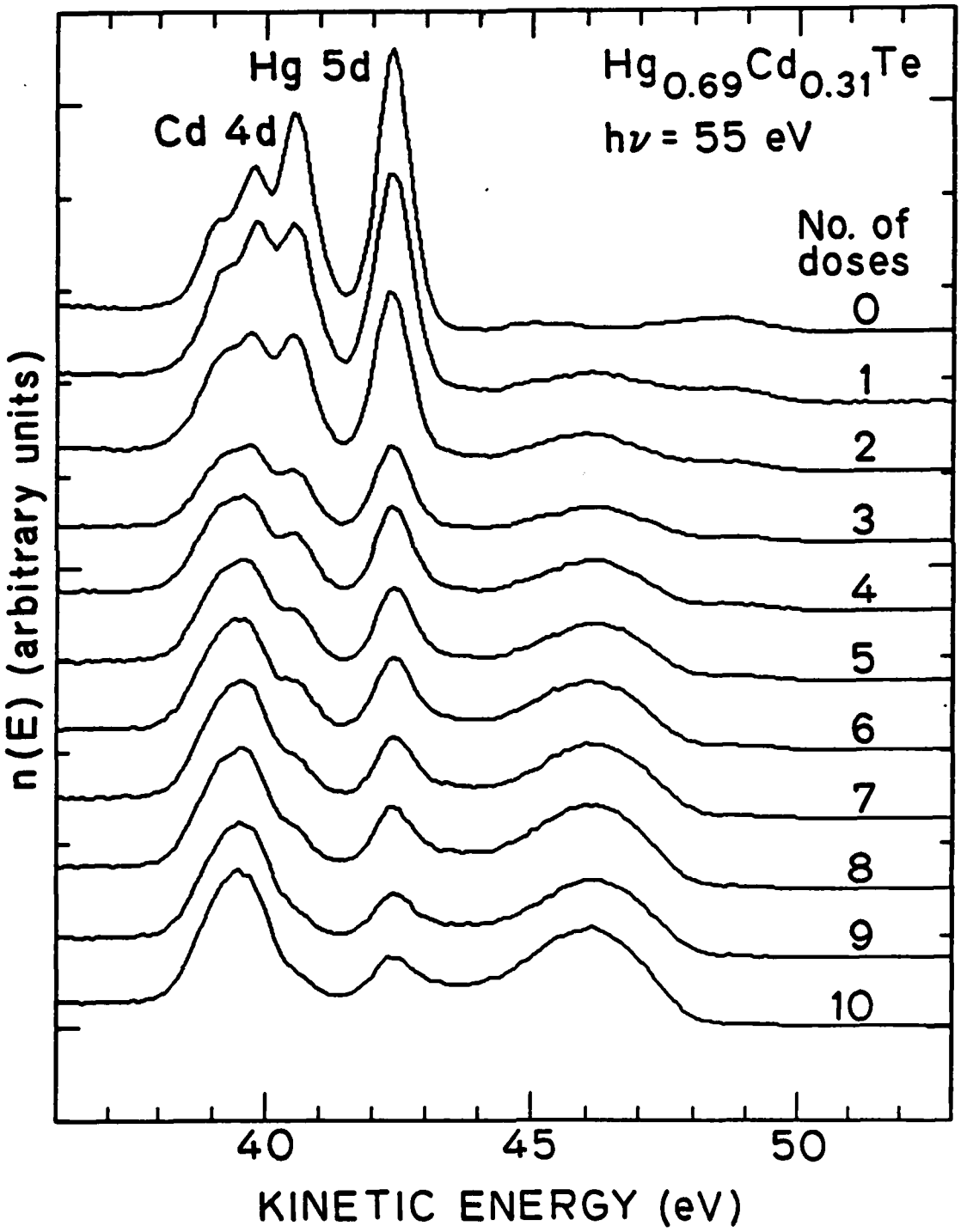
Hg 5d
Cd 4d
$Hg_{0.69}Cd_{0.31}Te$
hν = 55 eV
No. of doses
0
1
2
3
4
5
6
7
8
9
10
n(E) (arbitrary units)
40
45
50
KINETIC ENERGY (eV)

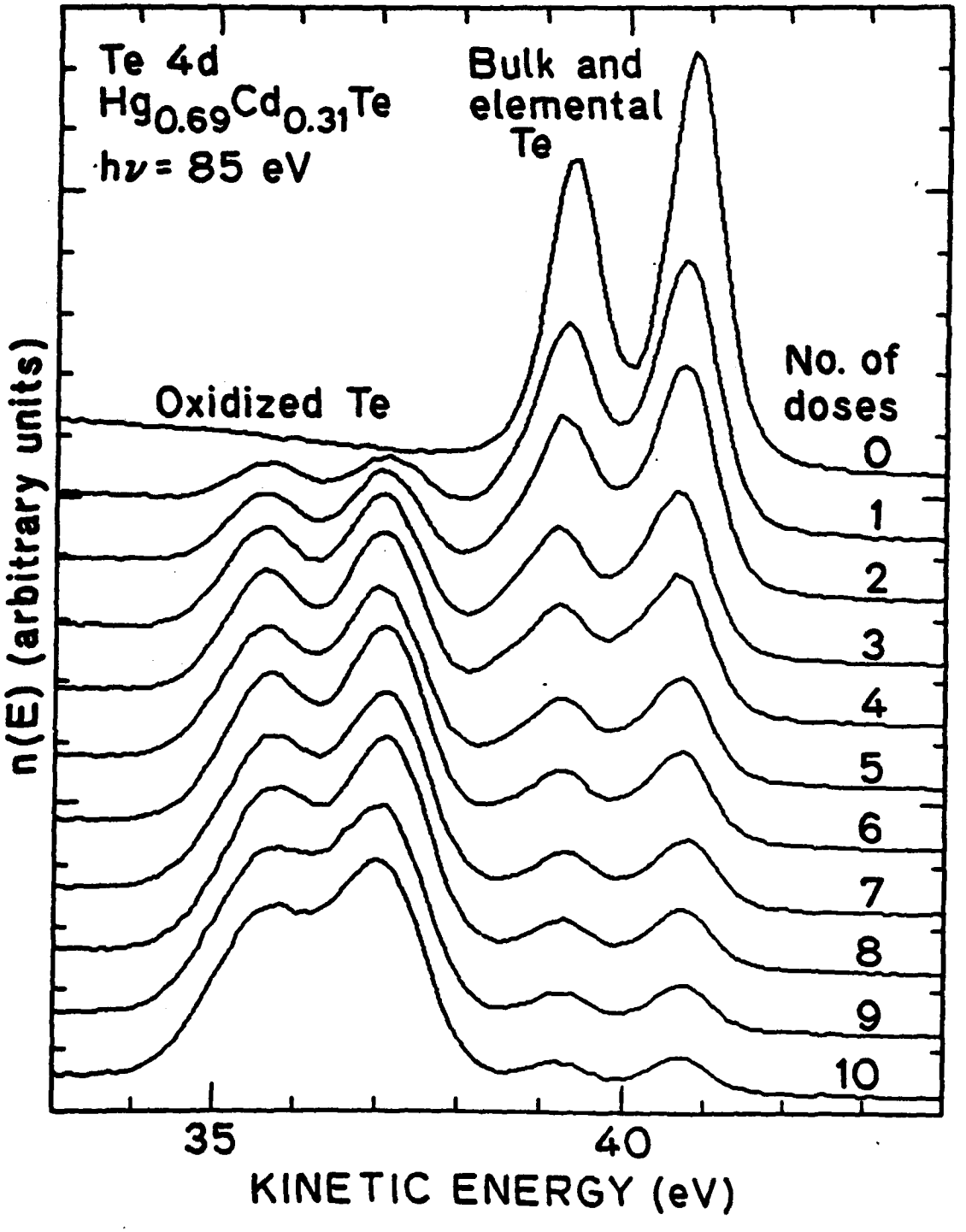
Te 4d
$Hg_{0.69}Cd_{0.31}Te$
$h\nu$ = 85 eV
Bulk and elemental Te
Oxidized Te
No. of doses
0
1
2
3
4
5
6
7
8
9
10
n(E) (arbitrary units)
35
40
KINETIC ENERGY (eV)

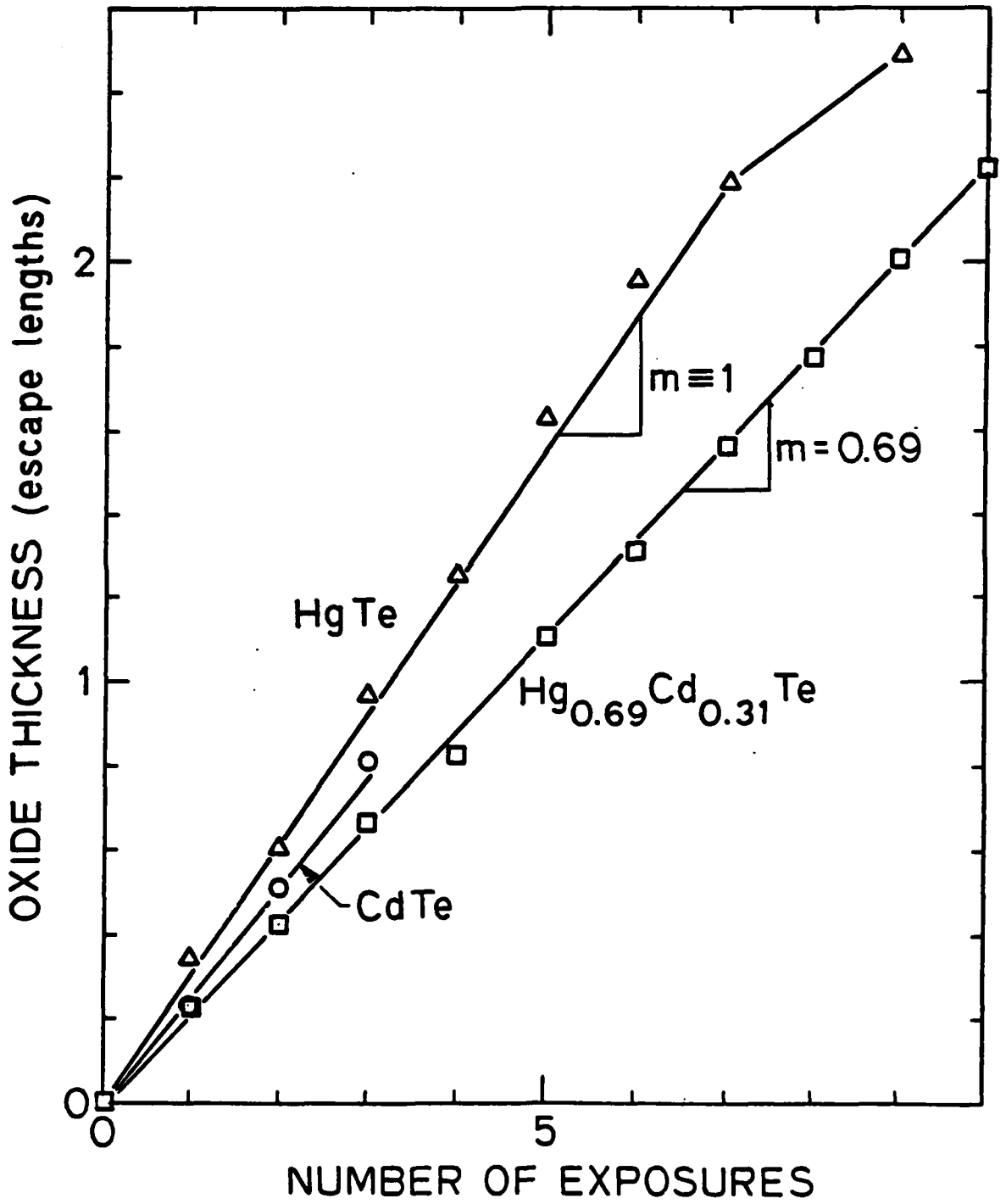
OXIDE THICKNESS (escape lengths)
NUMBER OF EXPOSURES
0
1
2
5
m ≡ 1
m = 0.69
HgTe
Hg0.69Cd0.31Te
CdTe

Section III-5

Low Temperature Cleavage of MCT.

A) Motivation

A large body of work in this program has been performed on the (110) face of MCT formed by cleaving unannealed solid state recrystalized material in vacuum. Despite the 10^{16} to 10^{17} cm^{-3} p-type character of the samples, measurement of the Fermi level position at the surface most often indicates an n-type surface.[1] The type conversion is due to defects created by the cleavage. A high density of dislocations has been observed at the edges of steps formed on the cleavage surface where the cleave jumps from one (110) plane to another.[2] While sites associated with such dislocations may not themselves be electrically active, the observation of these extended defects clearly indicates the energy to significantly perturb the lattice is available upon cleaving.

One means to reduce the possibility of defect creation is to reduce the temperature of the sample at the time of cleavage. In a study of the mechanical properties of MCT[3], Cole observed a strong temperature dependence of the yield stress for temperatures above room temperature. By cooling, the material may harden sufficiently that fracture occurs only along a single (110) plane.

B) Results of Initial Attempt at Low Temperature Cleavage.

An ultrahigh vacuum smple manipulator for use with the angle-resolving chamber was fabricated with the capability to cool and moderately heat cleavable samples transfered into the vacuum system from air. So that the low temperature of the sample could be maintained at the time of cleavage, the cleaver, consisting of a flat annealed copper anvil against which the sample rests and a sharp tungsten carbide blade driven by a linear motion feedthrough, was modified so that liquid nitrogen cooling could be applied to the anvil. The x=0.2 MCT sample used achieved a minimum temperature of 150 K. Because the anvil was warmer, the temperature at the time of cleavage was ~210 K. The resulting surface had a visible morphology and surface potential (the surface was n-type) which fell within the

distribution of results achieved to date at room temperature.

The constructed manipulator will prove of great utility in extending studies of oxygen uptake or metal deposition to temperatures other than room temperature. It will make possible experiments relating to Hg loss or surface structure which in fact require heating or cooling. An effort will be made to improve the performance of the cooling system of the cleaver and to repeat the low temperature cleaving experiment.

References

1. P.M. Raccah, U. Lee, J.A. Silberman, W.E. Spicer, and J.A. Wilson, Appl. Phys. Lett. 42 (1983) 374.

2. Semiannual Technical Report of this program, July 1, 1983.

3. S. Cole, A.F.W. Willoughby, and M. Brown, J. Crystal Growth 59 (1982) 370.}

(This Page Intentionally Left Blank)

Section IV

Alloy Bonding

Section IV-1

A number of calculations of properties of semiconductor alloys with emphasis placed on the II-VI compounds involving HgTe have been started. These calculations include:

1. determination of the many body generalizations of the atomic term values, electron extraction energies and many body excitation energies for all the group II, III, IV, V, and VI elements that are important in tetrahedral semiconductors. Their use in place of traditional term values takes account of the influence of some important correlation effects on semiconductor bond energies;

2. calculation of the bond energies of the "pure" semiconductor compounds and the modifications of these energies in pseudo-binary alloys;

3. calculation of the bond length changes in alloys and deviations from Vegard's law;

4. initiation of theory of vacancy formation that includes effects due to relaxation and charge redistribution around the impurity;

5. extension of Harrison's theory of the shear coefficients to dislocation energies in pure compounds and alloys;

6. devising of a theory of the hardness of semiconductors and their alloys; and

7. working out an improvement in the theory of the energy positions (deep states) of impurities in pure semiconductors and alloys.

Not all these calculations are completed, but several are in a stage worth reporting. In Section IV-2 the current status of our work on bond energies and lattice constants will be presented. Section IV-3 has a discussion of dislocation energies and hardness. Conclusions, recommendations based on them, and future plans are presented in Section IV-4.

Section IV-2

BOND ENERGIES AND LENGTHS IN AN ALLOY

The theory of the bond energy shifts in an alloy that was presented in our mid-year report[1] has now been refined and extended. All the important III - V and II - VI compounds have been treated. The details of these calculations will be prepared as a technical paper. The most important results are summerized in Figures (II - 1) and (II - 2) where the shift of a given type bond energy (e.g. HgTe) due to having one bond of a different type (e.g. CdTe) in one of the three adjacent bonds are presented. These energy shifts for now include only the largest terms; those that arise from local charge redistribution in the alloy. There are smaller terms due to bond length and bond angle distortions that must still be included to complete this calculation.

Figure II - 1 is a compilation of these bond energy shifts for the III-V compounds and Figure II - 2 is a similar plot for the II - VI compounds. For each bond type, e.g. GaAs, the lines under a cation denote the energy shift if one of the three neighboring bonds coupled to the anion have its cation replaced by different atom e.g. Al. A positive energy shift is destablizing and a negative shift is stablizing. An ordering Al,Ga,In for the cations, and P,As,Sb for the anions is used. An arrow under Ga pointing to the right means In and to the left means Al. A double arrow means move two steps in the indicated direction. Thus in the alloy $Al_{1-x}Ga_xAs$ according to this figure the GaAs bond is destablized by ~ 43 meV by an AlAs neighboring bond, and the AlAs bond is stablized by ~ 46 meV. If there are two neighboring

ALLOY MODIFICATION OF BOND ENERGIES FOR III-V COMPOUNDS

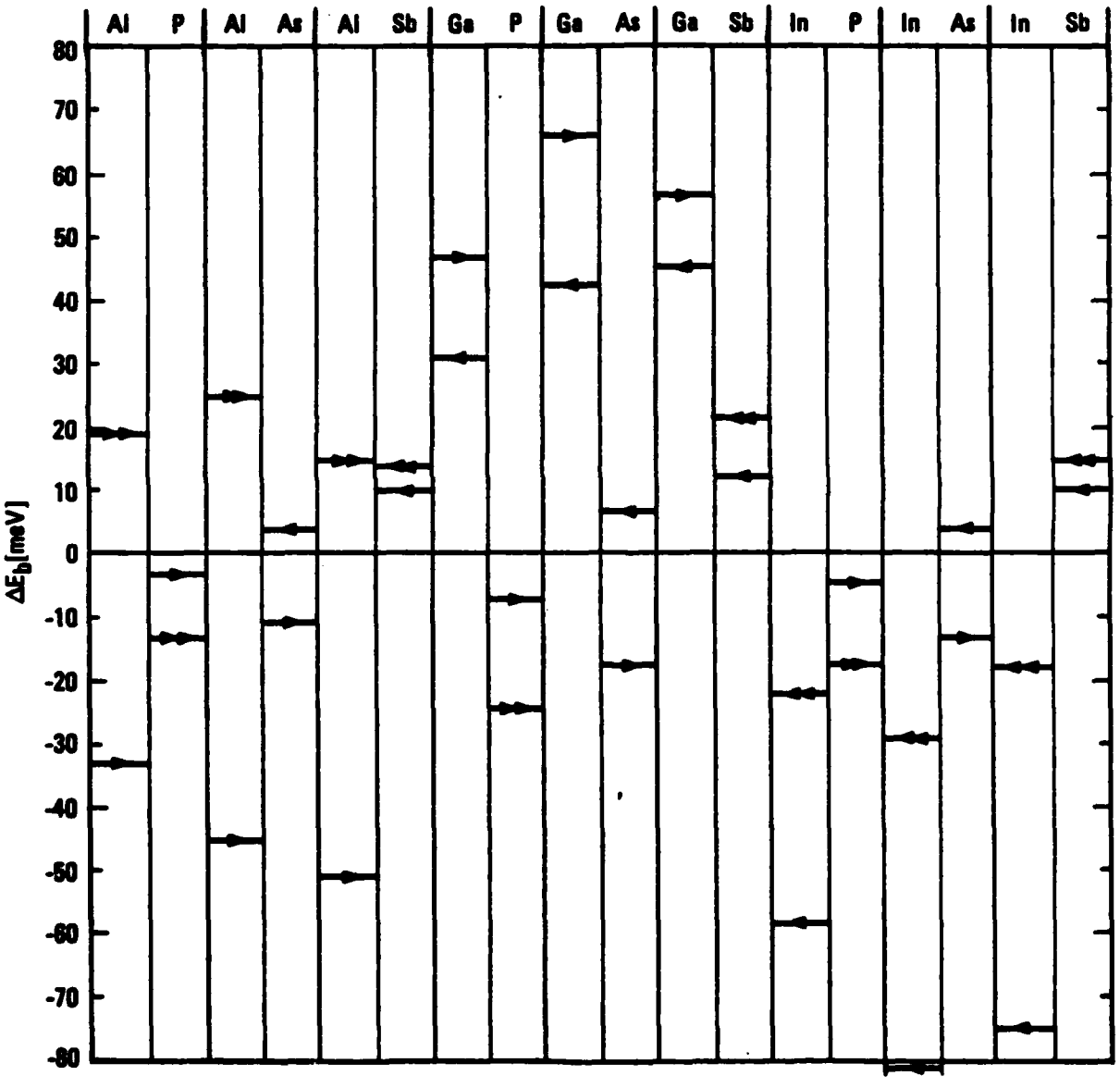

ALLOY MODIFICATION OF BOND ENERGIES FOR II-VI COMPOUNDS

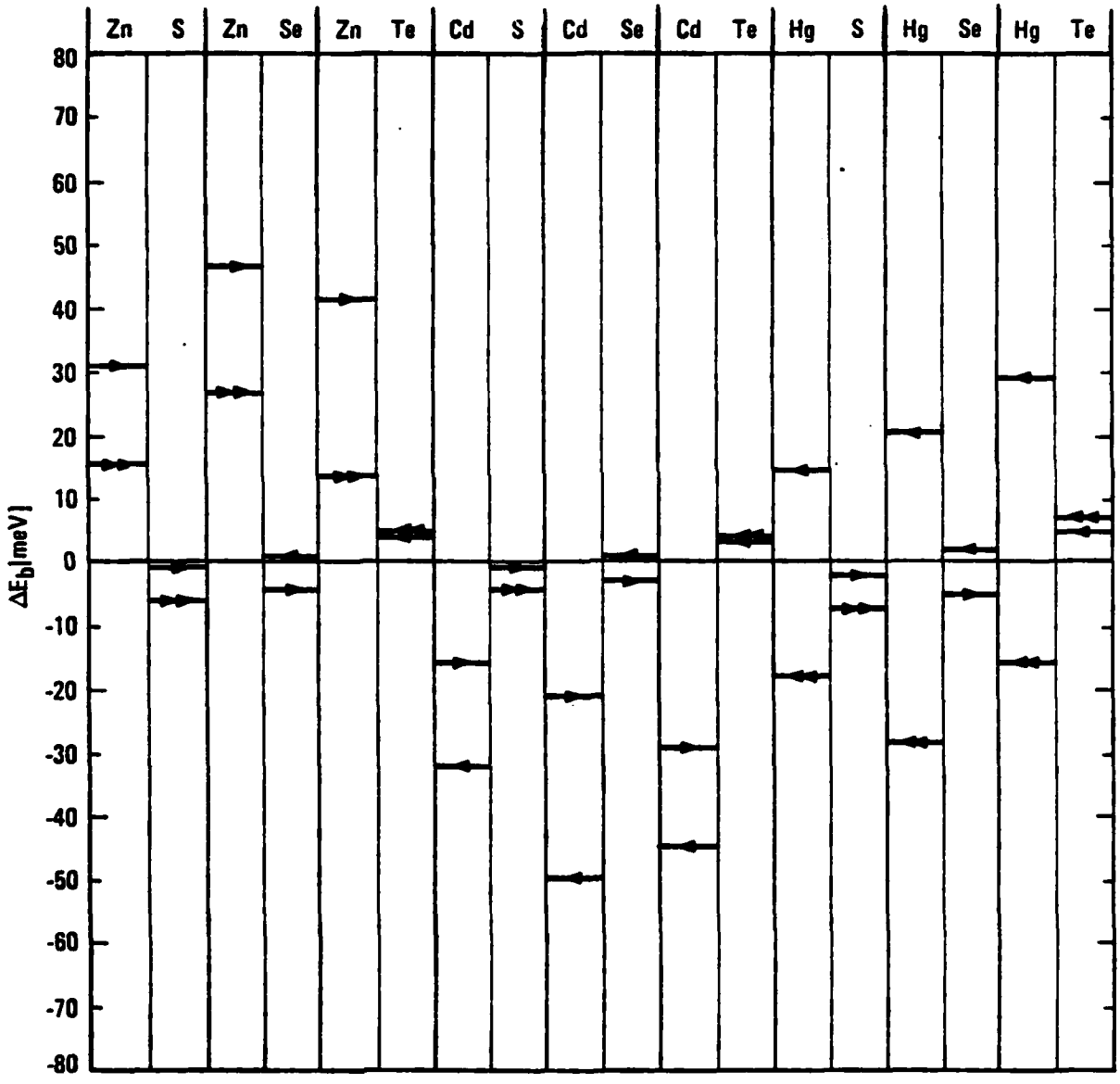

bonds with the different atoms these numbers roughly double, and for three they triple.

Focus now on Fig. (II-2_ and in particular the HgTe bond. This bond is destablized by ~30 meV per neighboring CdTe bond and ~5 meV per neighboring HgS or HgSe bond. However, the bond is stablized by ~16 meV per neighboring ZnTe bond. Since according to these calculations the bond strength of HgTe is only -0.480 eV, in a $Hg_{1-x}Cd_xTe$ alloy where a given HgTe bond is surrounded by three CdTe bonds its bond energy is reduced by 25%. This can have a substantial effect on a Hg vacancy formation energy. We have estimated the Hg Schottky defect formation energy in HgTe to be 0.78 eV, and the presence of Cd could reduce this to as little as 0.3 eV. It is unlikely to find this large a reduction in an alloy with $x \simeq 0.2$. However, in an alloy with x near unity the Hg vacancy formation energy could be quite small. This could have disasterous consequences to the stability of CdTe solar cells where a low concentration of HgTe is added to slightly reduce the bandgap. While the consequences are not so severe in the concentration range used in infrared detector applications, they are still potentially troublesome. We suspect this effect helps account for the ease with which Hg vacancies are found to form in the alloy.

If one calculates the bond length changes due only to effects caused by the charge shifts which are driven principally by the differences in the ionic properties of the bonds then they all shift in the wrong direction compared to experiment. Experiments on GaInAs have shown that in the alloy the bond lengths of the pure materials tend to be preserved but the shorter

GaAs bond expands slightly (~2%) and the longer InAs bond contracts by ~2%. The charge shift contribution yields the correct order of magnitude but the wrong sign. The charge shift term has a large effect on the metallic contribution to the bond energy. But this contribution is a small one. There is inherent in the bond length change the necessity for bond angle distortions and a change in the average bond lengths to allow the lattice to fit together. These bond angle distortions cause small changes in the covalent contribution to the bond energy, but this contribution is a large one. Once the bond angle distortion terms are included the bond length changes tend to reverse their sign. To obtain answers the calculation must be done self consistently, permitting the average lattice spacing to take on its proper value. Instead of simple algebraic expressions, the answers now require a computer program that itterates to self consistent results. We shall report the details of these calculations when they are completed.

If one adopts a model in which the spring constants associated with a bond are supposed to retain their pure crystal values in an alloy, then it can be demonstrated that the bond length shifts have the observed sign and magnitude. This model also accounts for the observed small deviations from Vegard's law in which the average bond length as a function of alloy concentration bows down slightly from a straight line projection. At present we have no theoretical justification for a conserved spring constant model, but the fact that it gives the correct answers is instructive.

Section IV-3

SEMICONDUCTORS AND THEIR ALLOYS: DISLOCATIONS AND HARDNESS

Dislocations in semiconductors are detrimental to device function, serve as channels for impurity migration and trapping which causes non uniform doping and degrades p-n junctions. They also decrease the material's resistance to plastic deformation. The aim of this paper is to provide insights into the underlying physical mechanisms controlling dislocations and the hardness of semiconductors and their alloys; and then to suggest strategies for decreasing dislocation densities. It is well established that the hardness of tetrahedrally coordinated semiconductor materials, Group IV, III-V and II-VI compounds exhibit a sharp variation with their near neighbor distance d, approximately proportional to d^{-9} for one group of seven compounds.[2] (The lattice constant, a, and d are related by $d = \sqrt{3}a/4$.) Thus, semiconductors with small lattice constants tend to be harder materials. These same materials have larger stiffness coefficients[3] and have fewer dislocations in as-grown crystals.[4,5,6] The composition x variation of the hardness of semiconductor alloys $A_{1-x}B_x$ bows up from a straight line projection between the respeceive hardnesses of the pure constituents.[2] The composition variation of the lattice constant of alloys bows down from the Vegard's rule straight line projection between those of the constituents.[7] We shall now interrelate these observations and some other more recent measurements, through an extension of Harrison's theory of the bonding of these semiconductors.[8]

The major reason for the properties just described can be understood qualitatively as follows. These materials have a low coordination number

with only four near neighbors. There are three contributions to their bonds. The most important one is the covalent energy that results from the interactions between the sp^3 hybrids on the different sites. The strength of this interaction is directional dependent and bond angle distortions require energy. The ionic contribution to the bond strength is fairly isotropic and adds little to the shear coefficients per bond. In crystals with higher coordination the ionic contribution to shear coefficients is more important. The metallic contribution to the bond energy is in this case also bond angle dependent. In metals (usually fcc, or bcc structures) with high coordination numbers this term dominates the shear coefficients. The shear coefficients (combinations of C_{44} and $C_{11}-C_{12}$) depend on crystal orientation and in Harrison's notation[7] are proportional to $V_2^3/d^5(V_2^2 + V_3^2)^{3/2}$ and $V_2 \sim d^{-2}$. V_2 is the covalent and V_3 the ionic energy in this notation. Thus in a case where the covalent energy dominates ($V_2 \gg V_3$) the shear coefficients are proportional to d^{-5}, while in the other limit they are smaller and proportional to d^{-11}.

There are two contributions to the dislocation energy per unit length[9] a short ranged core energy and a long range elastic energy arising from an integral over the energy of small bond angle distortions distributed over many sites.[9] The elastic contribution is typically ~ 5 times larger than the core energy and while the elastic term dominates, the core should not be completely neglected. However, in this treatment where the major trends are being sought we shall do so. The distortion energy per unit length is proportional to the product of a shear coefficient and the square of the Burger's vector.[9] The magnitude of the Burger's vector is porportional to the lattice constant, hence $E_D \sim V_2^3/d^3(V_2^2 + V_3^2)^{3/2}$.

Hardness is determined by applying a known force, F, to a probe of a prescribed shape driving it into the surface of the sample.[1] The area, A, of the resulting indentation is measured, and the hardness is the force per unit indented area. Many dislocations must be formed to allow the probe to indent the semiconductor. If the indenter is a rectangular pyramid where the angle between the normal to the point and an edge is θ, then the major contribution to the hardness is

$$H = \frac{F}{A} = \frac{Fh}{Ah} = \frac{\epsilon_T}{Ah} \tag{3-1}$$

where ϵ_T is the work required to cause the indenter to penetrate to a depth h. A side view of the indentation in a cut through its center is illustrated schematically in Figure (3-1). The top of the indentation has side length W so $A = W^2$. The Burger's vector has magnitude b which is approximately equal to the bond length d. The number of dislocations N_h required to accommodate an indentation to depth h is

$$N_h = \frac{h}{b} = \frac{W \cot\theta}{2b} \tag{3-2}$$

where θ is the angle between the normal to the tip of the indenter and a side. The edges of the extra atom planes that are driven from the indented volume into the bulk of the semiconductor are shown as lines in the figure. The ends of these lines are the positions of the dislocations which are perpendicular to the plane of the figure. The planes driven to the sides each have a finite extent and a trapazoidal shape. The planes dirven down under the indenter have a square shape.

Most of the work done on the indentor goes into the energy to form the dislocations. There are two major contributions to this energy. The first is the energy needed to form each dislocation and the second is the interaction

SCHEMATIC OF AN INDENTATION INTO A SEMICONDUCTOR

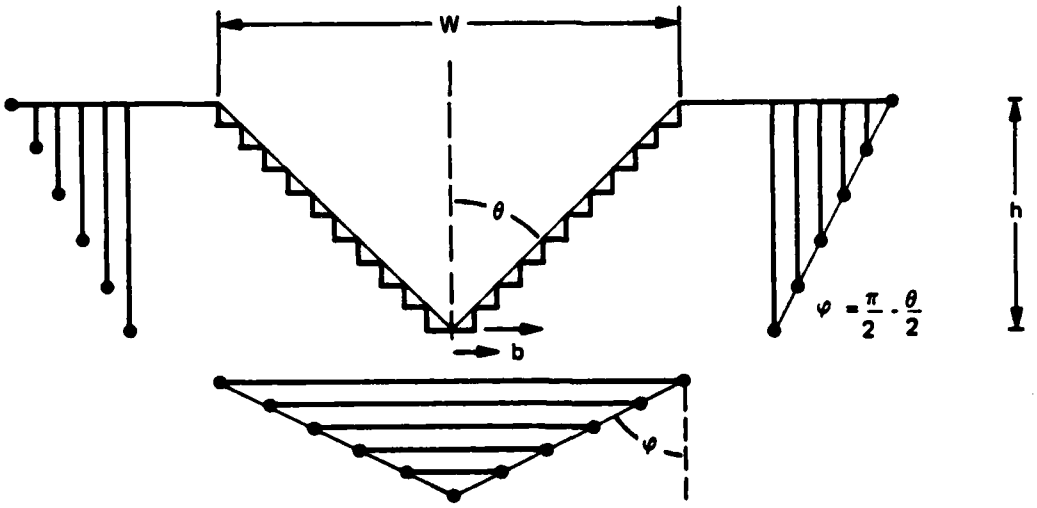

Figure 3-1

energy among these dislocations[9]. Since the extra planes driven to the sides of the indentation have a finite extent there are both edge dislocations at their base and screw dislocations associated with their termination. The square planes driven below the indentation have edge dislocations around the sides and screw dislocations at the corners to make the turns. Moreover, there are interactions among the dislocations which can produce a minimum energy configuration. For the kind of situation depicted in Figure (3-1) it always costs energy to position a second dislocation on a parallel glide plane to one already present. However, the magnitude of this extra energy can be minimized, and for proper configurations of the dislocations there are attractive forces along the glide planes that will tend to position the dislocations into the minimum energy configuration. The minimum configuration arises when half the atoms from the indented volume go respectively to the side and below the indenter. Then in both regions the maximum angle made between successive close-spaced dislocation lines and their glide planes is $\varphi = \pi/2 - \theta/2$ as shown in the figure. This is the minimum energy configuration. As we shall demonstrate shortly the minimum energy configuration is evidently established when soft materials are indented, but hard ones are more apt to align in a configuration closer to a maximum energy configuration where all the atoms go either to the sides or below the indenter.

An approximate expression for the energy required to indent the material is

$$\epsilon_T = 2.4\left[\sum_{i=1}^{N} E_i L_i + \frac{1}{2}\sum_{i,j=1}^{N}{}' E_{ij}\left\{\min(L_i, L_j)\right\}\right] . \qquad (3\text{-}3)$$

In the first term, the energy per unit length to form an eige dislocation is

$$E_i = \frac{Gb^2}{4\pi(1-\nu)} \ell n R/r_o, \tag{3-4}$$

the shear coefficient is G, the Burger's vector $b = d/\sqrt{3}$ for an indentation along a ⟨100⟩ axis, the range of the dislocation R is taken equal to W (for want of a better approximation) $r_o \approx d$ is the dislocation core radius, the Poisson ratio $\nu \cong 0.2$ for most semiconductors, and L_i is the length of the i'th dislocation. In the second term, E_{ij} is the interaction energy per unit length between dislocations i and j assuming they have parallel glide planes

$$E_{ij} = \frac{Gb^2}{2\pi(1-\nu)}\left[\ell n (R/r_{ij}) + \cos^2\varphi_{ij}\right] \tag{3-5}$$

r_{ij} is the separation between dislocation i and j, and φ_{ij} is the angle a line perpendicular to the dislocations and joining them makes with the glide plane as shown in Fig.(3-1). Since the various dislocations in a region have different lengths, the net interaction energy is approximated by multiplying the energy per unit length by the length of the shorter one. The 1/2 multiplying this term prevents double counting and the prime on the sum indicates that terms with i = j are to be omitted. The upper limits on the sums N are the number of dislocations in one region (side or bottom) associated with one edge. For the minimum energy configuration $N = N_h/2$. The four that multiplies the bracket accounts for the four sides, and the two for the two regions for each side.

We now encounter our first surprise. The energies per unit lentgh E_{ij} and E_i have comparable magnitudes. Since there are $\sim N^2$ terms in the interaction energy sum, only N terms in the formation energy sum, and N is a large number typically $\sim 10^5$, the interaction energy completely dominates the hardness. Hence neglecting terms due to screw dislocations core energies, and other

effects that influence the first term are unimportant. However, care must be taken with the interaction terms. In Eq. 3-3, a number of secondary interactions are neglected, some positive and others negative. These will be added later. The principal neglected terms are the interactions between two regions on each side (positive), and the interactions between adjacent side (and bottom) regions (positive, and the interaction between the opposite sides in the bottom regions (negative). Comparison of the results with experiment will tell us how important these neglected terms are likely to be.

The length of the i'th dislocation will be taken as

$$L_i = W \frac{N-i}{N} ; \quad i = 1,2,3,\ldots,N . \tag{3-6}$$

This is the largest length of the side inserted planes and its choice partially accounts for interactions between the otherwise neglected screw dislocations. The distance $r_{ji} = r_i - r_j$ is given by

$$r_{ij} = 2\sqrt{2}b|i - j| ; \; i,j = 1,2,3,\ldots,N \tag{3-7}$$

for the minimum energy configuration and a tetrahedrally bonded semiconductor. Finally in the indicated configuration

$$\varphi_{ij} = \varphi = \frac{\pi}{2} - \frac{\theta}{2} \quad \text{for all i, and j.} \tag{3-8}$$

Inserting these expressions, Eqs. (3-5), (3-6), (3-7), and (3-8), into the sums in Eq. (3-9) yields expressions of the form

$$\sum_j{}' \ln(R/r_{ij}) \left\{\min(L_i,L_j)\right\} = \frac{W}{N} \sum_{j=1}^{i-1} - \ln\left[\xi(i-j)\right] (N - j)$$

$$: \frac{W}{N} (N - i) \sum_{j=i+1}^{N} - \ln\left[\xi(j-i)\right]$$

$$\simeq \frac{W}{N}\left\{(N-i)\, i\left[-\ell n\,(\xi i)+1\right] + \frac{i^2}{2}\left[-\ell n\,(\xi i)+\frac{1}{2}\right]\right\} \tag{3-9}$$

where

$$\xi \equiv 2\sqrt{2}b/R \ll 1 \tag{3-10}$$

and only terms of order N^2 are retained in Eq. (3-9).

Similarly one finds

$$\sum_j \min\left\{L_i, L_j\right\} = \frac{W}{N}\left[\sum_j^{i-1}(N-j) + (N-i)\sum_{j=i+1}^{N} 1\right]$$

$$\simeq \frac{W}{N}\; N^2 - Ni + i^2/2 \tag{3-11}$$

Combining these results yields

$$e_T \simeq \frac{2Gb^2}{\pi(1-\nu)}\;\frac{W}{N}\;\sum_{i=1}^{N}\left\{(N-i)\, i\left[-\ell n\,(\xi i)+1\right] + \frac{i^2}{2}\left[-\ell n\,(\xi i)+\frac{1}{2}\right] + \cos^2\varphi\left[N^2 - Ni + i^2/2\right]\right\}$$

$$\simeq \frac{2\,Gb^2WN^2}{3\,\pi\,(1-\nu)}\left[-\ell n\,(\xi N) + \frac{11}{12} + 2\cos^2\varphi\right] \tag{3-12}$$

and for the minimum hardness

$$H_{min} = \frac{G\cot\theta}{12\pi(1-\nu)}\left[-\ell n\left(\frac{\cot\theta}{\sqrt{2}}\right) + \frac{11}{12} + 2\sin^2\frac{\theta}{2}\right] \tag{3-13}$$

One can also get a number for the hardness of a dislocation configuration in which all the material is either pushed to the side or the bottom. In this case the factor of 2 in front of Eq. (3-3) is removed, $N - N_h$, $\xi = \sqrt{2}b/R$, and $\varphi = \pi/2 - \theta$. Then a non-equilibrium maximum hardness

in the context of this model, is obtained (remember that some terms have been neglected)

$$H_{max} = \frac{G \cot\theta}{3\pi(1-\nu)} \left[-\ell n\left(\frac{\cot\theta}{\sqrt{2}}\right) + \frac{11}{12} + 2\sin^2\theta \right] \tag{3-14}$$

The proper answer for most materials lies somewhere between H_{min} and H_{max}. For an indenter with $\theta = \pi/4$ we have

$$H_{min} = 0.0414 \frac{G}{1-\nu} \tag{3-15}$$

and $H_{max}/H_{min} = 5.80$. Harrison[3] has shown that

$$G = 2.38 \frac{\hbar^2}{m} \frac{\alpha_c^3}{d^5} \left[\frac{\text{joules}}{m^3}\right] \tag{3-16}$$

where $\hbar$ is Planck's constant over 2π, m is the free electron mass ($\hbar^2/m = 1.220 \times 10^{-38}$ [joules $-m^2$]), α_c is the covalence $\alpha_c = V_2/(V_2^2 + V_3^2)^{1/2}$, and d is the bond length. Combining Eqs. (3-14) and (3-16), using $\nu = 0.2$, and changing the dimensions to those in terms of which experimental hardness numbers are customarily quoted gives

$$H_{min} = 1.23 \times 10^4 \frac{\alpha_c^3}{(d\,[\text{Å}])^5} \left[\frac{\text{kgm}}{(\text{mm})^2}\right] \tag{3-17}$$

Values calculated from Eq. (3-17) and H_{max} along with the corresponding experimental values H_{exp} are given in Table (3-1) and the theoretical versus the experimental results are plotted in Fig. (3-2) for a number of typical semiconductors.

The plot in Fig. (3-2) has the minimum and maximum theoretical values of H at the two ends of the vertical lines for each compound plotted as a function of the corresponding experimental values. If the theory were perfect

Table 3-1

Experimental and Theoretical Values of the Hardness of Several Semiconductors in Units of $[kgm/(mm)^2]$

Material	d[Å]	$-V_2$[eV]	V_3[eV]	α_c	H_{min}	H_{max}	H_{exp} (a)
Ge	2.450	4.081	0	1	138	803	1000
AlSb	2.657	3.470	1.480	0.9198	72.0	418	350
GaP	2.359	4.403	1.998	0.9106	127	736	910
GaAs	2.448	4.088	1.851	0.9110	106	613	700
GaSb	2.639	3.518	1.243	0.9429	80.2	465	520
InP	2.541	3.795	2.292	0.8560	72.6	421	469
InAs	2.623	3.561	2.146	0.8565	62.0	360	360
InSb	2.805	3.112	1.538	0.8965	50.9	295	220
ZnSe	2.455	4.065	3.791	0.7313	53.8	312	137
ZnTe	2.643	3.507	3.014	0.7584	41.4	240	82
CdTe	2.805	3.114	3.141	0.7040	24.6	143	56
HgTe	2.797	3.132	2.941	0.7290	27.8	161	26

(a) With the exception of the HgTe value all numbers are from reference 1. The HgTe numbers are from reference 9.

THEORETICAL AND EXPERIMENTAL HARDNESS VALUES

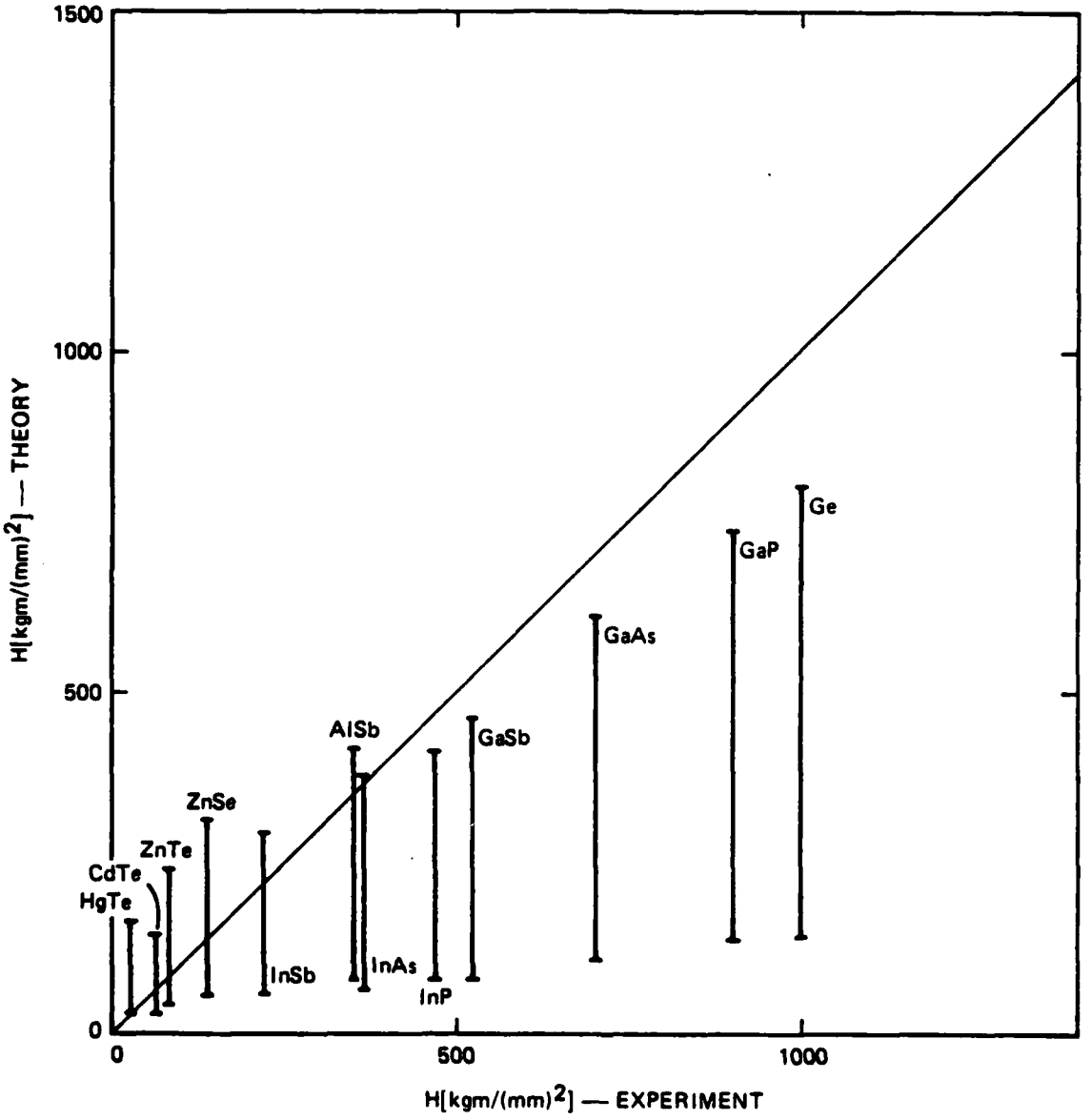

Figure 3-2

and the experimental values were accurate the points would fall on the indicated unity slope line. There are several conclusions that can be drawn from Fig. (3-2). First the order of magnitude of the predicted and measured values are the same. Second the trends from one compound to another are properly given by the theory. The H_{min} values are generally too small, but they fit the soft materials better, and H_{max} fits the harder materials better. As we have pointed out some terms have been neglected that will very likely increase H_{min} (and H_{max}), but they should be smaller than those retained.

The semiconductor alloys exhibit a composition variation of their hardness that bows up relative to the straight line virtual crystal behavior.[2] Moreover the peak in the bowed curve is in general shifted toward the higher hardness side of the curve. The bond length of alloys had, until recently, been thought to vary nearly linearly with composition (Vegard's law) between those of the alloy constituents. The deviations of the average bond length from the simple concentration weighted average behavior has a downward curvature. However, new EXAPS measurements on $Ga_{1-x}In_xAs$ clearly display an entirely new behavior. The bond lengths of the constituents remain nearly constant in the alloy. While the longer one, GaAs, becomes shorter and the shorter one, InAs, becomes longer as the alloy composition changes, they each change by less than 2% of their pure crystal values. In order for the crystal to accommodate the resulting microstrains and for an alloy in which the cation is the substitutional constituent, the cation sublattice retains its face centered crystal structure and the anions adjust their positions according to their near neighbor configuration. For example, if an As cation has three In neighbors and one Ga neighbor, it will shift along a (1,1,1) direction toward the Ga neighbor. One can show that for an $A_{1-x}B_x$ alloy the average bond length $\bar{d}$ is given to lowest order by

$$\bar{d} \cong (1-x)\, d_A + x\, d_B + 3x\,(1-x)\,(\Delta d_A^1 + \Delta d_B^1) \qquad (3\text{-}18)$$

where d_j is the bond length of the pure compound of type j = A,B, and Δd_A^1 is the shift in bond length of bond A in a configuration in which there are three A bonds and one B bond (an A(3)B(1) configuration). The first two terms are Vegard's law which says that the bond lengths vary linearly between those of the pure constituents. The correction bowing term depends on the algebraic sum of the bond length changes for A(3)B(1) and A(1)B(3) configurations. We have done a literature search on measurements of $\bar{d}(x)$ and found that in all cases where deviations from Vegard's law have been determined the average lattice constant bows down, so $\Delta d_A^1 + \Delta d_A^1$ is negative. This correlates well with the experimental finding that hardness bows upward since from experiment H is roughly proportional to d^{-9}. Thus a large part of the bowing of the hardness of semiconductor alloys (sometimes called alloy hardening) correlates with the extra energy required to form dislocations and other mechanisms e.g. dislocation pinning at impurity sites, often invoked to explain this kind of phenomena in metals probably play a minor roll in semiconductors.

Dislocations are often found in materials as they are grown. Their density is determined by the strains to which they are subjected in the growth process, and the cool down schedule. A dislocation constitutes an excitation relative to the perfect crystal ground state. At the elevated grown temperature the number of dislocation present is controlled by equilibrium thermodynamics. As the crystal is cooled, a critical temperature is reached where the time required for the dislocations to equilibrate

AD-A146 343 HGCDTE SURFACE AND DEFECT STUDY PROGRAM(U) SANTA BARBARA RESEARCH CENTER GOLETA CALIF J A WILSON ET AL. JAN 84 SBRC-41514 MDA903-83-C-0108 2/2

UNCLASSIFIED F/G 20/12 NL

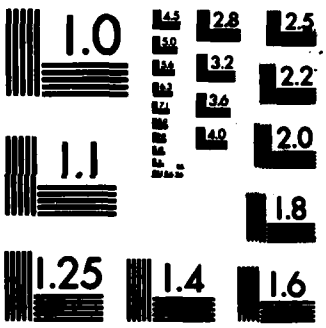

MICROCOPY RESOLUTION TEST CHART
NATIONAL BUREAU OF STANDARDS-1963-A

becomes long compared to annealing times so the population of dislocations is frozen. For some systems the critical temperature may be the growth temperature. In any case one expects materials with similar growth temperatures to have fewer dislocations if E_D is larger. This expectation is confirmed in the recent work reported on $Zn_{1-x}Cd_xTe$ bulk material. The best CdTe that has even been grown has dislocation densities in excess of 5×10^5 cm^{-2}. The addition of only 4% Zn reduced the dislocation count to less than 5×10^4 cm^{-2}. The ZnTe bond length is 2.643 Å while the CdTe bond length is 2.805 Å, a 6% difference. This 6% difference in bond length translates into a 2% difference in the dislocation energy per unit length for 1-x = 0.04. Dislocation energies for typical lengths are $\sim$ 10 eV, so a 2% increase corresponds to $\sim$ 0.2 eV. Using a critical dislocation freeze in temperature of 800°C this yields a population decrease of $\sim$ 20. These estimates demonstrate that the observed factor of 10 reduction in the dislocation density of the $Zn_{0.04}Cd_{0.96}Te$ alloy relative to that of CdTe lies in the range of values that can reasonably be expected.

The argument just presented naturally leads to a strategy for decreasing dislocations in other semiconductors. If an alloy is made of the material of interest with another compound with a shorter bond length then the dislocation density should be reduced. For example, this suggests that the addition of a small amount of GaP (d - 2.359 Å) may significantly reduce the dislocation density of bulk grown GaAs (d = 2.448 Å). It has been demonstrated that the addition of $\sim$ 1% GaN (d = 1.946 Å) to GaAs can yield a large volume of dislocation-free material.[5,6]

We have demonstrated that the dislocation energies, and hardness of tetrahedrally bonded semiconductors are rapid functions of the reciprocal of the bond length. The bond lengths of the different bonds in semicon-

ductor alloys nearly retain their pure cyrstal values, and the average bond length always bows down from Vegard's rule. This observation correlates well with the finding that the composition variations of the hardness of semiconductor alloys bows upward. Moreover, the rapid d dependence of dislocation energies explains the dramatic decrease of the dislocation density in bulk grown $Zn_{0.04}Cd_{0.96}Te$ material relative to that found in CdTe.

Section IV-4

IV CONCLUSIONS AND FUTURE PLANS

A theory of a number of material structural properties of semiconductor alloys has been established. This theory accurately predicts many of the observed trends, and even some quantitative results. For the focus material of this study $Hg_{1-x}Cd_xTe$ our major conclusions are

- Cd destablizes the already weak HgTe bond and has little effect on the dislocation energy.
- Zn both stabilizes the HgTe bond and increases the dislocation energy.

More generally for other alloys an important result is that if one has a material, e.g., GaAs, and one wishes to reduce the dislocation density is to alloy it with another material, e.g. GaP, GaN, BAs, with a shorter bond length. There is experimental evidence for several alloy combinations that confirms the utilizy of this strategy.[4,5,6] Obviously one must not go to such a high alloy concentration that the electronic properties of the host are badly degraded.

The plans for our future work include the following tasks:

1) Complete the alloy bond length shift calculation,
2) Complete the vacancy formation energy calculation and extend it to find diffusion coefficients,
3) Improve the accuracy of the hardness theory and extend it to alloys,
4) Determine the mechanism driving the thick region of misfit dislocations found between CdTe substrates and epitaxial HgCdTe layers,

5) Establish the relation between alloy bonding properties and optical phonon mode frequencies,

6) Begin calculating the structural properties of alloy surfaces,

7) Finish calculating the energy levels of deep impurity states in HgCdTe alloys.

REFERENCES

1. J.A. Wilson, W.E. Spicer, J.A. Silberman, A. Sher, and R.G. Wilson (See in particular Section 3) "HgCdTe Surface and Defect Study Program" Interim Technical Report Contract No. MDA-903-83-C-0108, July 1983.

2. N.A. Goryunova, A.S. Borshchevskii, and D.N. Fretiakov "Semiconductors and Semimetals" Vol. 4, Ed. R.K. Willardson and A.C. Beer (Academic Press, New York, 1968) ch. 1.

3. W.A. Harrison "Electronic Structure and the Properties of Solids" (Freeman, San Francisco, 1980); R.C. Sokal "Thesis, Stanford University 1978"; W.A. Harrison, "Microscience" Vol. 4,p34, 1983 (limited distribution, SRI International publication).

4. S.L. Bell and S. Sen, IRIS Detector Specialty Group Meeting, Boulder Colorado, 1983; T.W. James and B.F. Zuck, Ibid.; T. MacGee (private communication).

5. Y. Seki, H. Watanabe, and J. Matsui, J.Appl. Phys.,42,822(1978).

6. G. Jacob, J.Crystal Growth 59, 669 (1982).

7. The lattice constant variation with composition bowes downward in $Hg_{1-x}Cd_xTe$, $GaAs_{1-x}Sb_x$, $Al_{1-x}Ga_xN$, $CdSe_{1-x}S_x$, $InP_{1-x}As_x$, $GaP_{1-x}As_x$, $Ga_{1-x}In_xP$, and $Ga_{1-x}In_xAs$. The references are too numerous to list. We have found no cases in which the lattice constant bows upward.

8. W.A. Harrison, Phys. Rev. B, 27, 3592(1983).

9. J.W. Christian "Theory of Transformations in Metals and Alloys" 2nd Ed.)Pergamon, New York, 1975) Ch. 7. For a discussion of the interaction energies, see pages 262-263.

10. S. Cole, M. Brown, and A.F.W. Willoughby "The Microhardness of $Cd_xHg_{1-x}Te$" (private communication).

11. J.C. Mikkelsen,Jr., and J.B. Boyce, Phys. Rev. Lett, 19, 1412 (1982).

Acknowledgements

We wish to acknowledge many helpful discussions with T.N. Casselman, R. E. Kvaas, D. R. Rhiger and C. E. Jones. We especially acknowledge the technical assistance of R. E. Cole and C. R. Curtis for bulk crystal growth, M. H. Kalisher for LPE growth, M. S. Langell for wafer preparation and MIS fabrication as well as many helpful comments and finally to J. F. Santarosa and M. E. Boyd for their assistance with device testing.

We are also appreciative of the many collaborations which have aided this work, specifically, W. A. Harrison, A-B Chen, P. M. Raccah, F. Pollack and S. Perkowitze. Finally we are grateful for the support and encouragement of the program sponsor R. A. Reynolds and the technical monitor R. A. Graft.

(This Page Intentionally Left Blank)

END

FILMED

10-84

DTIC